Journal Pre-proofs

Ji Li, Zhixian Cao, Yifei Cui, Xuanmei Fan, Wenjun Yang, Wei Huang, Alistair G.L. Borthwick

Please cite this article as: Li, J., Cao, Z., Cui, Y., Fan, X., Yang, W., Huang, W., Borthwick, A.G.L., Hydro-Sediment-Morphodynamic Processes of the Baige Landslide-induced Barrier Lake, Jinsha River, China, *Journal of Hydrology* (2021), doi: https://doi.org/10.1016/j.jhydrol.2021.126134

This is a PDF file of an article that has undergone enhancements after acceptance, such as the addition of a cover page and metadata, and formatting for readability, but it is not yet the definitive version of record. This version will undergo additional copyediting, typesetting and review before it is published in its final form, but we are providing this version to give early visibility of the article. Please note that, during the production process, errors may be discovered which could affect the content, and all legal disclaimers that apply to the journal pertain.
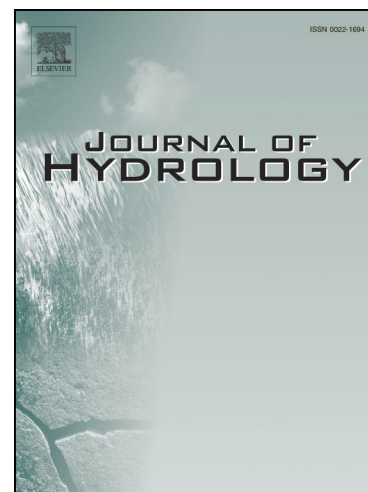
Hydro-Sediment-Morphodynamic Processes of the Baige Landslide-induced Barrier Lake, Jinsha River, China

Ji Li[a, b], Zhixian Cao[a] *, Yifei Cui[c], Xuanmei Fan[d], Wenjun Yang[e],

Wei Huang[e], Alistair G. L. Borthwick[f]

[a] *State Key Laboratory of Water Resources and Hydropower Engineering Science, Wuhan University, Wuhan 430072, China*;

[b] *Zienkiewicz Centre for Computational Engineering, College of Engineering, Swansea University, Swansea SA1 8EN, UK*;

[c] *State Key Laboratory of Hydroscience and Engineering, Tsinghua University, Beijing 100084, China;*

[d] *State Key Laboratory of Geohazard Prevention and Geoenvironment Protection, Chengdu University of Technology, Chengdu 610059, China*;

[e] *Changjiang River Scientific Research Institute, Wuhan 430010, China*;

[f] *Institute for Infrastructure and Environment, The University of Edinburgh, Edinburgh EH9 3FG, UK.*

*Corresponding author, Zhixian Cao, email address: zxcao@whu.edu.cn

Highlights:

- The 2018 Baige landslide-induced barrier lake on the Jinsha River is investigated

- The whole process is well reconstructed by a single 2D model for the first time

- An artificial flood channel effectively alleviated downstream flood risk

- Grains drive water during landslide dam formation, but water governs the outburst

- Effects of upstream inflow discharge and initial landslide volume are revealed

Abstract

A large landslide impacting a river may cause a multi-phase chain of hazards, comprising landslide-generated waves, inundation as a barrier lake develops upstream a landslide dam arising from rapid sediment deposition, and downstream flooding due to barrier lake outburst. Two major landslides (each of volume ~ 10^7 m^3) occurred successively on 10th October and 3rd November 2018 at Baige village, Tibet, China. Both landslides led to a natural dam that completely blocked the Jinsha River, along with a barrier lake filled with upstream river inflow. Although the first barrier lake breached naturally, a significant quantity of residual material from the first landslide dam was left behind without being eroded. After the second landslide occurred, a flood channel was urgently constructed to facilitate an artificial breach of the barrier lake as it formed. The Baige landslide-induced barrier lake is unique as triggered by two successive landslides and outbursts a mere five weeks apart. Here a computational investigation is presented of the hydro-sediment-morphodynamic processes of the Baige barrier lake, using a recent 2D double layer-averaged two-phase flow model. This is the first modelling study of the whole field and whole processes for the formation and outburst of a landslide-induced barrier lake as well as the resultant floods, without evoking presumptions on dam breach (which have prevailed for decades and bear much uncertainty). The computed results agree well with field observations in terms of landslide-generated waves, landslide dam morphology, stage and discharge hydrographs at the dam site and downstream flood hydrographs. The artificial flood channel is shown to be effective for alleviating downstream inundation. Water and grain velocities are demonstrated to be distinct, characterizing the primary role of grains in landslide dam and barrier lake formation and the dominant role of water in barrier lake outburst and the resultant flood. Relatively low inflow discharge and large initial landslide volume favour landslide dam and barrier lake formation, but delay the outburst and downstream flood. The present 2D double layer-averaged two-phase model holds great promise for assessing future landslide-induced multi-hazard chains in rivers, and informing mitigation and adaptation strategies.

Keywords: landslide dam; landslide-generated waves; barrier lake outburst; flood; hydro-sediment-morphodynamic processes; double layer-averaged two-phase flow model

1. Introduction

Landslides are common geophysical mass events in mountainous regions, especially those with deep, narrow valleys (Costa and Schuster, 1988; Ermini and Casagli, 2003). A landslide impacting a river often produces a multi-hazard chain comprising landslide-generated waves, a landslide dam, a barrier lake, a lake outburst, and resultant floods, leading to spatial-temporal amplification of hazard (Carpignano et al., 2009; Fan et al., 2019a). More specifically, when a subaerial landslide impacts a narrow river valley, large amplitude water waves and active sediment transport can be generated. Due to rapid deposition of a huge amount of sediment, a landslide dam forms as the riverbed rapidly aggrades and then emerges from the water (Costa and Schuster, 1988; Van Asch et al., 1999). The resulting water waves may trigger further landslides and/or collapses of the opposite riverbank, entraining additional sediment into the river and facilitating landslide dam formation. As a consequence of sustained upstream inflow and significant water-level rise, the water impounded by a landslide dam usually creates a barrier lake, which may inundate upstream land and infrastructure. Owing to its rather loose structure, a landslide dam formed by granular materials can easily burst, leading to destructive downstream floods. Such outburst floods from a barrier lake consist of highly mobile water-sediment mixtures, capable of traveling long distances (sometimes beyond 100 km) at high velocity (exceeding 10 km/hr). These events can cause high numbers of casualties and severe infrastructural damage (Ermini and Casagli, 2003; Shang et al., 2003; Dai et al., 2005), due to their sudden onset, high magnitude discharge, long runout distance, and their tendency to flow along existing river channels where humans and property are concentrated (Carrivick, 2010; Cui et al.,

2013).

Typical historical examples include the landslide dam outburst events in June 1786 at the Dadu River, Sichuan, China, which is reported to have caused more than 100,000 fatalities (Dai et al., 2005; Lee and Dai, 2011), in October 1999 at the Poerua River, New Zealand (Davis et al., 2007), in April-June 2000 at the Yigong Zangpo River, Tibetan, China (Delaney and Evans, 2015), in May 2008 at Tangjiashan, Sichuan, China due to the Wenchuang earthquake (Xu et al., 2009), and in October 2018 at Yarlung Tsangpo River in Tibetan Plateau, China due to ice-avalanche (Chen et al., 2020). More recently, two major landslides occurred successively on 10 October and 3 November 2018 (Fan et al., 2019b), which created a natural dam that completely blocked the Jinsha River, followed by a barrier lake filled by upstream runoff. On 12 October, the first barrier lake breached naturally with a peak discharge of about 10,000 m^3/s (Cai et al., 2019). The residual landslide dam was replenished with sediment from the second landslide on 3 November, forming a larger barrier lake than the first. On 11 November, following the urgent construction of a flood channel, the second barrier lake breached artificially with a peak discharge of 33,900 m^3/s.

Modelling the whole-process chain of a landslide-induced barrier lake flood is important for two reasons. First, knowledge of the chain is useful in assessing the hazard and risk of potential future landslide-induced barrier lake flood events. This is both salient and timely, noting that climate change is promoting increased instability of high mountain slopes and has accelerated increasing trends in the amount, intensity, and occurrence frequency of extreme precipitation (Donat et al., 2013), which are likely to trigger more landslides. Second, the whole-process chain is key to improving our understanding of such earth surface processes

that are prohibitively difficult to observe in nature owing to their sheer complexity. Physically, a typical landslide-induced multi-hazard chain involves two distinct but intertwined processes: aggradation through sediment deposition during landslide dam and barrier lake formation; and degradation induced by sediment erosion during a barrier lake outburst and the subsequent floods. Previous studies have mostly focused on one or two components of the whole-process chain, whereas little work has been done on the whole-process chain modelling.

Landslide dam and barrier lake formation represent the first part of the whole-process chain. In general, existing models for resolving landslide dam and barrier lake formation can be divided into two categories: discrete models and continuum models. Typical discrete models like Smoothed Particle Hydrodynamics - SPH (Shi et al., 2016; Xu et al., 2020) and Materials Point Method two-phase models (Bandara and Soga, 2015) can be directly used for modelling landslide dam and barrier lake formation. Other examples include coupled Discrete Element Method landslide models and fluid flow models based on computational fluid dynamics (Zhao et al., 2017), Lattice-Boltzmann Method (Leonardi et al., 2016), as well as coupled Discontinuous Deformation Analysis and SPH models (Wang et al., 2017, 2019). Yet, excessive computational costs preclude applications of these models to real field-scale cases. As far as continuum models are concerned, although 3D models are available (e.g., Hu et al., 2020), double layer-averaged models hold great promise for resolving landslide dam and barrier lake formation due to their ability to represent the two-way coupling between landslide motions and water flows (Abadie et al., 2012) and to achieve a sensible balance between theoretical integrity and applicability (Li et al., 2019). It should be emphasized that

double layer-averaged models are automatically applicable when there is only a single-layer flow, either clear-water flow or water-sediment mixture flow. Recently, a 2D double layer-averaged two-phase flow model (Li et al., 2020) has been proposed for landslide dam and barrier lake formation, which employs one set of layer-averaged single-phase flow equations to describe the upper clear-water flow layer and a second set of layer-averaged two-phase flow equations to describe the subaerial or subaqueous water-sediment mixture flow layer. This model incorporates multiple grain size, inter-phase and inter-grain size interactions, unlike previous double layer-averaged models that involve a single-phase flow assumption and assume a single grain size (e.g., Skvortsov and Bornhold, 2007; Liu and He, 2016; Si et al., 2018; Li et al., 2019) and that ignore mass exchange with the bed, sediment mass conservation and steep slope effect (e.g., Skvortsov and Bornhold, 2007; Si et al., 2018). It is noted that the double layer-averaged single-phase model by Liu and He (2016) incorporated mass exchange with the bed, but incorrectly added a term for actual momentum exchange with the bed (see statement by Cao et al. 2017), and assumed constant sediment concentration, which is in conflict with the sediment mass conservation law.

Overtopping flow with subsequent dam erosion is the most common trigger for a barrier lake outburst (Costa and Schuster, 1988). Over the past few decades, substantial effort has been devoted to improving the understanding of the mechanisms underpinning a barrier lake outburst and the subsequent flood (Cao et al., 2011b). Particular attention has been paid to landslide dam breaching due to its governing role in the generation and propagation of the downstream flooding. According to ASCE/EWRI (2011), dam breach models can be categorized as parametric models, simplified physically based models, and detailed

physically based models. Parametric models are derived purely from data collected from a series of documented breaching events (e.g., Walder and O'Connor, 1997; Xu and Zhang, 2009; Peng and Zhang, 2012). Simplified physically based models, such as NWS BREACH (Fread, 1988), WinDAM (Temple et al., 2005), HR BREACH (Morris et al., 2009), DABA (Chang and Zhang, 2010), and DLBreach (Wu, 2013), predict outflow hydrographs from a breaching dam. The accuracy of such predictions hinges upon predefined model assumptions (most critically, weir flow assumption) and physical input parameters. Detailed physically based models (Wang and Bowles, 2006a, b; Faeh, 2007; Wang et al., 2008; Cao et al., 2011b, c; Wu et al., 2012; Huang et al. 2012; Li et al. 2013) incorporate the physical mechanisms of a dam breach. Discharge and stage hydrographs as well as breach development can be resolved without predefining or constraining the evolution process. It is noted that in order to predict outburst downstream floods, it is customary for the aforementioned parametric and simplified physically-based dam breach models to be integrated with flood routing models, e.g., FLO-2D (O'Brien et al., 1993), HEC-RAS (USACE, 2016), and BASEMENT (Vetsch et al., 2018). In contrast, detailed physically based models can resolve flow and sediment transport throughout the entire computational domain (ASCE/EWRI, 2011).

Integrated modelling refers to individual modelling of specific processes within a whole-process chain, with sub-model outputs of a single process used at each subsequent step as input to the next process sub-model. A general disadvantage of this approach is that transitions between different processes are not straightforward (Worni et al., 2014), and one sub-model output may not exactly fit the required input for the next sub-model. Concurrently, integrated modelling hinges upon the capability of the sub-models involved. Liu and He

(2018) tried to model the whole-process chain of the Yigong landslide by integrating a double layer-averaged single-phase model (Liu and He, 2016) for landslide dam and barrier lake formation and a conventional single layer-averaged single-phase model (e.g., Cao et al., 2004) for a dam breach and subsequent flood routing. Fan et al. (2020a) conducted an integrated modelling study on the Baige landslide-induced multi-hazard chain using a MassFlow sub-model for landslide movement, a DABA sub-model (Chang and Zhang, 2010) for dam breaching, and a one-dimensional HEC-RAS sub-model for downstream flood routing. Inevitably, the integrated model is constrained by the capability of each sub-model. For instance, the MassFlow sub-model is a single layer-averaged single-phase flow model for landslide movement, and so cannot resolve landslide-induced waves and barrier lake formation that involve strong interactions between landslide motion and river flow.

Overall, a single state-of-the-art model that properly couples all physical processes is the way forward (Worni et al., 2014). In this regard, a 2D double layer-averaged two-phase flow model appears particularly attractive, noting that such a model has previously been applied successfully to landslide dam and barrier lake formation caused by a landslide impacting a river (Li et al., 2020), and that its single-phase predecessor was applied for a barrier lake outburst and subsequent flood (Li et al., 2013). Here the hydro-sediment-morphodynamic processes of the Baige landslide-induced multi-hazard chain are investigated using the model of Li et al. (2020). First, we aim to benchmark the model against field observations of landslide-generated waves, landslide dam morphology, stage and discharge hydrographs in 2018. The role of water and grains in the whole processes is evaluated. Second, we aim to unravel the effects of inflow discharge and landslide volume on the multi-hazard chain as

unstable rock mass clusters in the source area of the Baige landslides may fail in the future, characterizing potential for river damming and flooding (Fan et al., 2020a). To the authors' knowledge, this is the first whole-field and whole-process modelling study of the Baige landslide-induced multi-hazard chain using a single physically based model (Li et al., 2020), unlike existing studies on a part of the whole-process chain (Hu et al., 2020; L. Zhang et al., 2019; Zhong et al., 2020; Fan et al., 2020a). Most notably, the present work does not involve presumptions regarding the onset of landslide dam outburst and of the breach/scour pattern and discharge estimation by analogy to weir flow, which have prevailed for several decades and bear excessive uncertainty.

2. Baige barrier lake

In 2018, the Jinsha River, the upper course of the Yangtze River, was blocked by two successive landslides that occurred on 10 October and 3 November (Fig. 1). At 22:00 on 10 October (Beijing time, UTC + 8 throughout the paper), a large landslide occurred on the right bank of the Jinsha River, at Baige village, located at the border between Sichuan Province and Tibet Autonomous Region, China (98°42′17.98″ E 31°4′56.41″ N). The first landslide had a total material volume of about 27.5 million m^3 (Cai et al. 2019), the majority of which formed a landslide dam of bed length ~1500 m and crest width ~ 700 m (Fig. 2a), aligned stream-wise and transverse respectively with the river. The dam crest elevation ranged from 3005 m above mean sea level at the left bank to 2931 m at the right bank. This landslide dam completely blocked the Jinsha River, for the first time in recent history. As the inflow

discharge reached 1680 m^3/s (Cai et al., 2019), the water level rose rapidly, leading to the formation of a barrier lake, called the "10.10" Baige barrier lake. The landslide dam overtopped naturally at 17:30, 12 October, and underwent breaching for about 21 hrs (Fig. 2b). Details of the breaching process have been documented as follows. The breaching flow discharge was less than 100 m^3/s before 20:00 on October 12. By 00:45 on October 13, the water level in the barrier lake reached a maximum of 2932.7 m above mean sea level, corresponding to a water storage volume of 290 million m^3. The overflow increased significantly after 01:00 on October 13. At 06:00 on October 13, the breaching flow peaked at about 10,000 m^3/s (Cai et al. 2019). Afterwards, the breaching flow gradually attenuated and returned to base flow by about 14:00 on October 13. The natural breach of the "10.10" Baige barrier lake resulted in a flood that caused huge damage to towns in its downstream path. Many houses, roads, and bridges were damaged or even destroyed, and more than 20,000 people had to be evacuated.

About 3 weeks after the natural breach of the first barrier lake, a second landslide, caused by reactivation of residual material left behind by the first landslide, occurred at the same site at 17:15 on 3 November. Landslide material was deposited on the earlier natural breaching channel and blocked the Jinsha River once again (Fig. 3a). The second landslide had an initial volume of about 3.5 million m^3, and an additional entrainment volume of about 8.5 million m^3. The average height of the new landslide dam was 50 m higher than its predecessor, and its lowest crest elevation was approximately 2966 m above mean sea level. With an incoming flow discharge of about 800 m^3/s, the water level increased continuously, forming the so-called "11.03" Baige barrier lake. As the second landslide had raised the overall height of

the landslide dam, the threat posed by the second barrier lake was higher than by the first lake. To mitigate flood risk, an artificial flood channel, 220 m long, 15 m deep, 42 m top width, and 3 m bottom width, was constructed at the lowest crest of the second landslide dam, reducing its bed elevation to 2951 m (Fig. 3b). With this flood channel in place, the landslide dam overtopped at 04:45 on 12 November, and the breaching process lasted over 50 hrs (Fig. 3c, d). The peak dam breach flow discharge reached 33,900 m^3/s at 18:20 on 12 November. At the dam site, the discharge returned to a base flow level by 08:00 on 14 November. The outburst flood destroyed many bridges along the Jinsha river including the Old Zhubalong Jinsha Bridge connecting a key highway between Sichuan and Tibet, inundated numerous towns, and led to the urgent evacuation of over 100,000 people.

The study area of the present work extends from approximately 6 km upstream of the Baige landslide dam site to Yebatan gauging station (54 km downstream of the Baige landslide dam site), and includes a ~ 60 km long reach of the Jinsha river (Fig. 1).
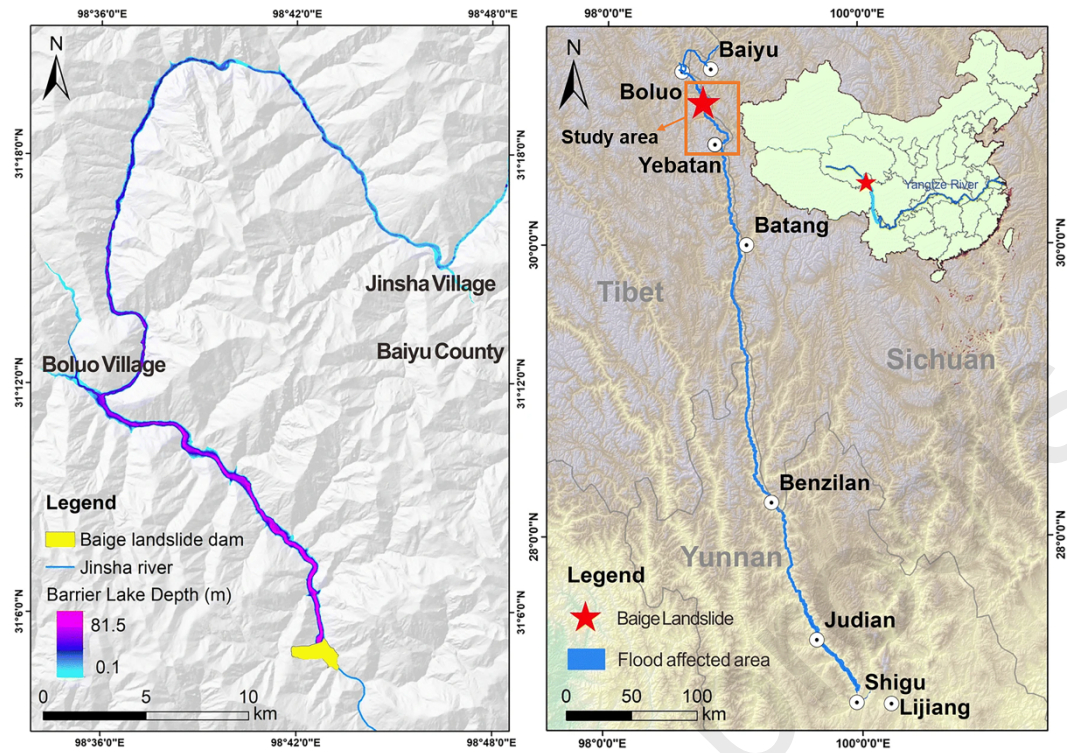
Fig. 1. Location of Baige barrier lake, Jinsha River, China (adapted from Fan et al., 2020a): (a) upstream areas inundated by barrier lake; (b) towns affected by downstream flooding (the orange box indicates the study area).

Fig.2. "10.10" Baige barrier lake: (a) formation; (b) after breaching. (photo courtesy of Chinanews.com).
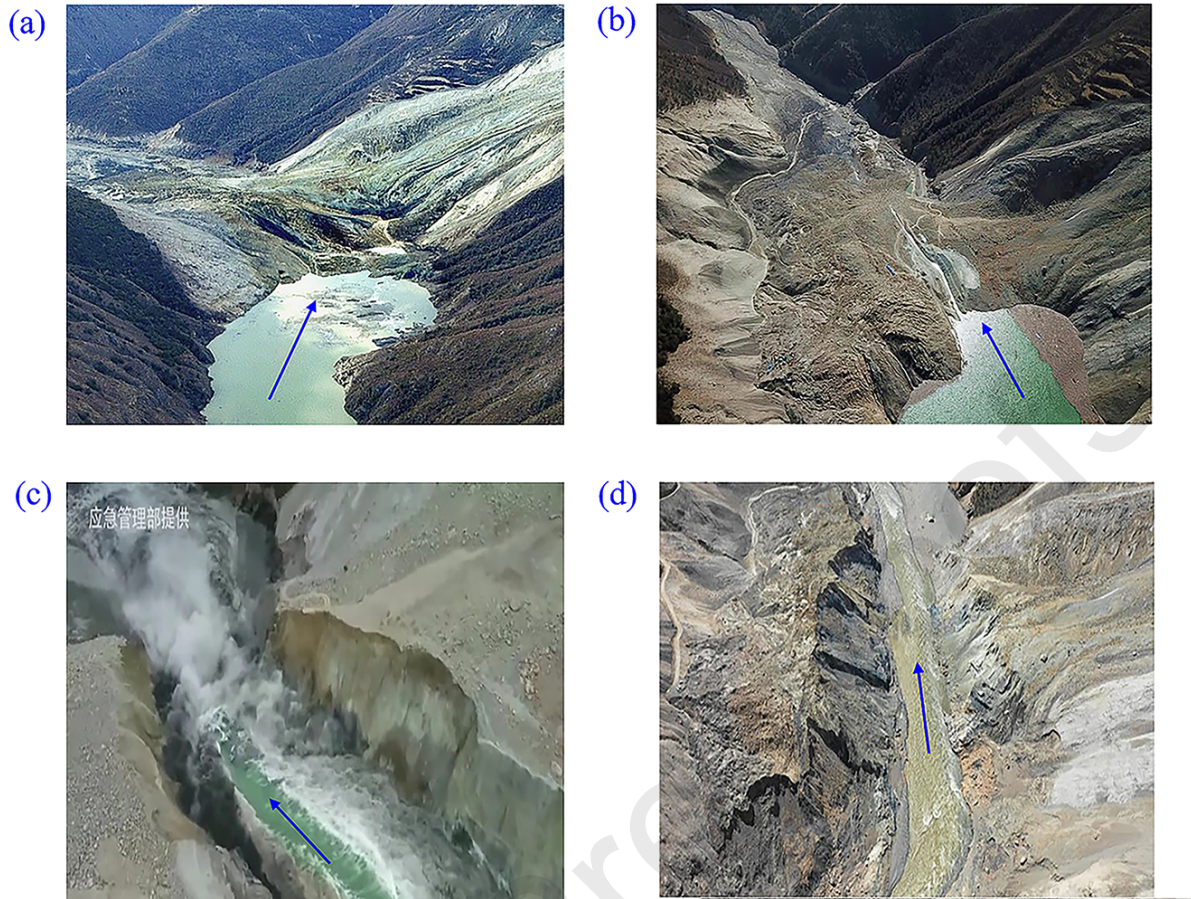
Fig. 3. "11.03" Baige barrier lake: (a) formation; (b) with artificial flood channel; (c) during breaching; (d) after breaching (photo courtesy of a CCTV.com; b Red Star News; c Ministry of Emergency Management of China; d L. Zhang et al., 2019).

3. Modelling method

3.1. Mathematical model

A recent state-of-the-art 2D double layer-averaged two-phase model (Li et al., 2020) is used to resolve the whole-process chain concerning the Baige events, commencing from landslide-generated waves, to landslide dam and barrier lake formation as the landslide impacted the Jinsha river, and thence to the outburst of the barrier lake and subsequent flood propagation downstream.

Li et al. (2020) provide a detailed description of the 2D double layer-averaged two-phase flow model equations, model closure, and the numerical algorithm. Briefly, the model has been constructed according to continuum mechanics principles, and explicitly incorporates multiple grain sizes, sediment mass conservation, mass exchange with the bed, and interphase and inter-grain size interactions. To close the model, a set of relationships is introduced to determine shear stresses, water entrainment, interaction forces, and sediment exchange fluxes. It should be noted that all the closure relations used in the double layer-averaged two-phase flow model have been established in the general field of shallow water hydro-sediment-morphodynamics. Although the model incorporates first-order factors, such as gravitation, resistance, inter-phase and inter-grain size interactions, higher-order factors such as non-Newtonian liquid viscous stress (Pudasaini, 2012), viscous particle resuspension (Reeks and Hall, 2001) and shear-induced particle migration (Morris, 2009), are yet to be included in the model.

3.2. Model set-up

In this study, in order to improve computational efficiency, the whole-process chain concerning the Baige barrier lake events of 2018 has been divided into Phase I: "10.10" Baige barrier lake event, and Phase II: "11.03" Baige barrier lake event. This is reasonable given the more than three-week gap between the two events. For Phase I, the pre-sliding bed topography was reconstructed using a 15m-resolution DEM (Digital Elevation Model). The total duration of the Phase I simulation was 72 hrs, from 22:00 on 10 October to 22:00 on 13 October. For Phase II, the bed morphology resulting from the first event was used as the

initial bed topography. The total duration of the Phase II simulation was 260 hrs, from 17:15 on 3 November to 13:15 on 14 November. For each phase, time $t = 0$ s coincided with the instant that the relevant landslide began to occur. The position and thickness of the initial landslide body were estimated from the post-landslide field survey (Cai et al., 2019). Water level elevation and velocity prior to landslide were determined by maintaining a constant base flow at the inlet boundary. From the landslide deposit investigation by L. Zhang et al. (2019), the bulk porosity $p = 0.45$, median grain size $d_{50} \approx 10$ mm, grain density $\rho_s = 2700$ kg/m³. According to the grain size distribution measured by L. Zhang et al. (2019), the sediment mixture was separated into two size fractions: $d_1 = 1$ mm (60%) and $d_2 = 20$ mm (40%), with mean diameter d_m of 8.6 mm.

The friction angle $\delta = 35°$, the Manning coefficients for bed roughness $n_b = 0.04$ m$^{-1/3}$ s, interface roughness $n_w = 0.01$ m$^{-1/3}$ s, the empirical weighting parameter $\varphi = 0.65$, and the modification coefficient $\phi = 1$ were calibrated to the observed landslide dam morphology and breaching flow discharge after the first landslide, and then directly applied to the second barrier lake event. The inflow discharge of clear water (Q_i) was kept constant throughout each phase of the simulation, i.e. $Q_i = 1680$ m³/s for Phase I, and $Q_i = 800$ m³/s for Phase II. The clear water velocity and layer thickness at the inlet were determined by the method of characteristics. At the outlet, either the method of characteristics was used to obtain updated values of the flow variables under subcritical flow conditions, or zero flow variable gradients imposed for supercritical flows (Liang and Borthwick, 2009). Within the time period considered, the landslides did not reach the computational boundaries, and so the landslide boundary conditions were simply set at the initial static state. The overall

dimensions of the computational domain were 35 km × 20 km, and a fixed uniform mesh of spatial increment 20 m was adopted. The $x-$ and $y-$ directions are aligned north-south and east-west, respectively. The Courant number, Cr, was set to 0.4.

To quantify the error of a numerical solution as compared with measured data, the non-dimensional discrepancy is defined based on the L^1 norm

$$L_f^1 = \frac{\sum_{i=1}^{N} abs(\overline{f}_i - \widehat{f}_i)}{\sum_{i=1}^{N} \overline{f}_i} \qquad (1)$$

where the symbol f represents physical variables such as bed deformation thickness and flow discharge; N is the number of measured data; $\overline{f}$ denotes numerical solution, whereas $\widehat{f}$ represents measured data.

4. Results

4.1. Phase I: the "10.10" Baige barrier lake event

First, the Phase I "10.10" Baige barrier lake event is reconstructed, commencing from landslide-generated waves, and landslide dam and barrier lake formation, through to the barrier lake outburst and downstream flood propagation. Multiple anticipated scenarios concerning effects of inflow discharge and initial landslide volume are considered, and sensitivity analysis to evaluate the effects of bed friction coefficient $\tan\delta$ and Manning roughness coefficient n_b are conducted.

4.1.1. Landslide movement and wave generation

According to the field survey and analysis of broadband seismograms undertaken by Z. Zhang et al. (2019), the peak velocity of the landslide during its runout was recorded at the nearest seismological station within 100 s. Fig. 4 shows the predicted evolution of landslide velocity U_m $(=\sqrt{u_m^2 + v_m^2}$, where u_m and v_m are the layer-averaged horizontal velocity components of the water-sediment mixture in the landslide in the $x-$ and $y-$directions. After initiation, the sliding mass accelerates eastwards down the hillslope alongside the Jinsha river, and first arrives at the water surface at $t=$ 20 s when the landslide front has a speed of approximately 62 m/s and has not yet reached its maximum (Fig. 4c). The rear of the landslide continues to push the front further into the river channel. By $t=40$ s, most of the landslide material has impacted the river and is generating waves; meanwhile, the direction of travel of the landslide material is diverted downstream with a maximum sliding mass speed of approximately 72 m/s (Fig. 4d). The predicted maximum speed is close to alternative computed results ($\approx$ 75 m/s) by Hu et al. (2020) using Flow-3D software. Subsequently, the landslide gradually decelerates, resulting in decreased landslide speed and thickness due to rapid deposition of the landslide material (Fig. 4(e-f)). Notably, at $t=$ 100 s, landslide movement has almost come to a halt with its maximum speed falling below 2 m/s, echoing the findings from the field survey and analysis of broadband seismogram signals (Z. Zhang et al., 2019). By $t=$ 900 s, the landslide thickness has almost vanished, indicating that most of the landslide material has been deposited on the riverbed and a landslide dam formed.

After the landslide impacts the Jinsha River, the river surface is disturbed, generating large waves. These landslide-generated waves are initially forced by inertia of the high-speed

sliding mass, with water displaced soon after the sliding mass crashes into the river channel. Along with the sliding mass, the generated waves tend to run up the opposite bank in the direction of the landslide run-out. After a landslide-generated wave moves to its maximum elevation on the opposite bank, water then flows back into the watercourse. As evident in Table 1, the computed results provide a satisfactory match to field observations by Cai et al. (2019) of the maximum run-up elevation of the landslide-generated waves and the size of the area affected by the waves on the opposite bank. Fig. 5 shows predicted water level hydrographs at Points A, B, and C along the river course, which indicate the propagation of landslide-generated waves downstream and upstream of the "10.10" Baige landslide in the Jinsha River. The hydrographs indicate that the waves propagate as bores with steep front and flatting rear. The maximum elevation of the water level at point B rise to 2950 m, exceeding the initial water surface by about 90 m. The maximum water level reaches 2919 m at point A and 2900 m at point C, indicating that the landslide-generated waves may produce more serious hazards in the downstream zone. The initial rises in water level at points B and C occur almost simultaneously, showing that the main entry position of the sliding mass is situated in the near upstream zone.
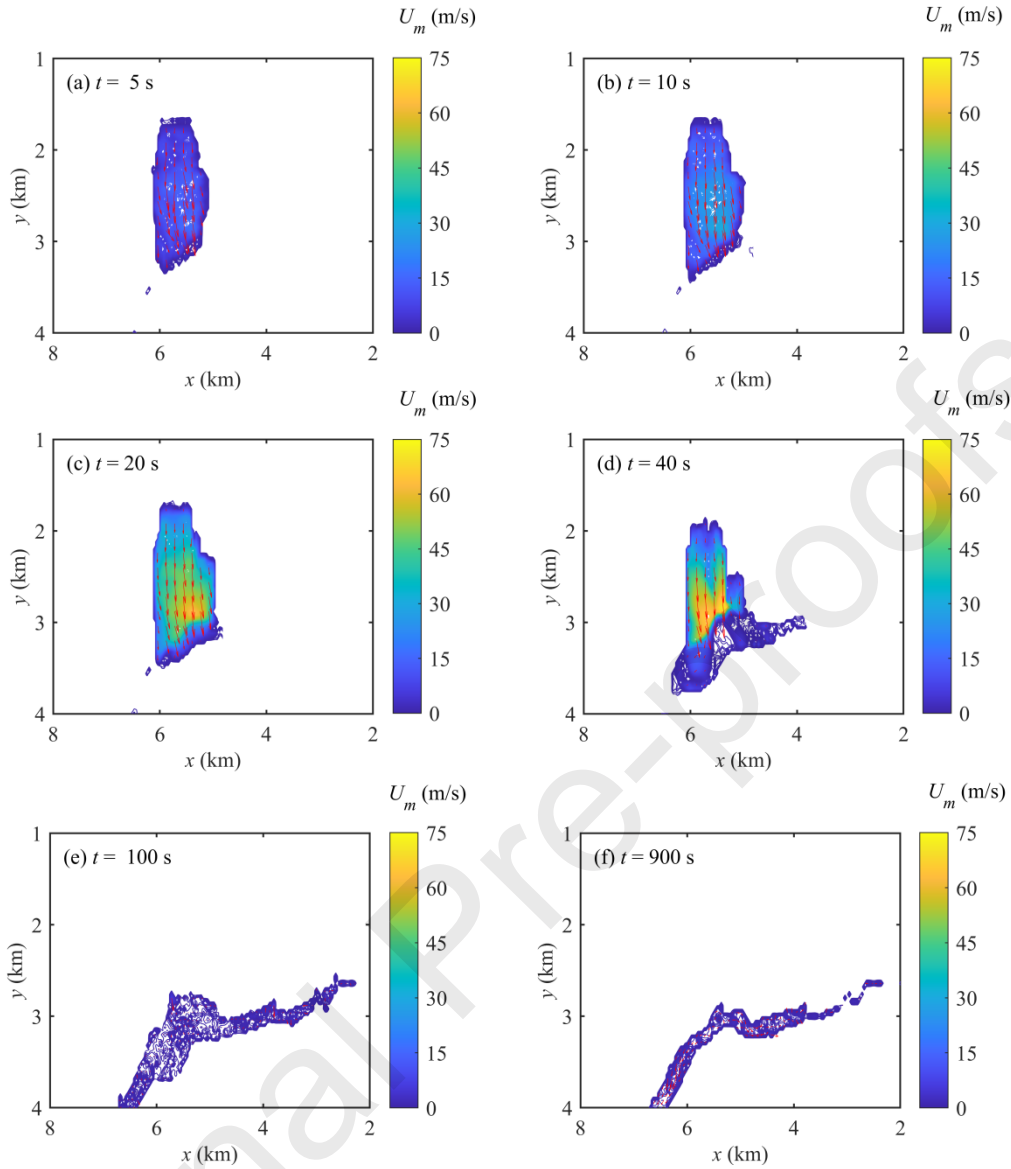
Fig. 4. Phase I "10.10" Baige landslide impacting Jinsha river: model predictions of landslide velocity field at times $t =$ (a) 5 s, (b) 10 s, (c) 20 s, (d) 40 s, (e) 100 s, and (f) 900 s.

Table 1 "10.10" Baige landslide-generated wave run-up on the opposite bank

Results		Computed	Measured
Maximum elevation (m)		3051.8	3065
Affected region	Length (m)	1690.5	1500
	Area (10^4 m^2)	36.3	37.6

* Observed data from Cai et al. (2019)
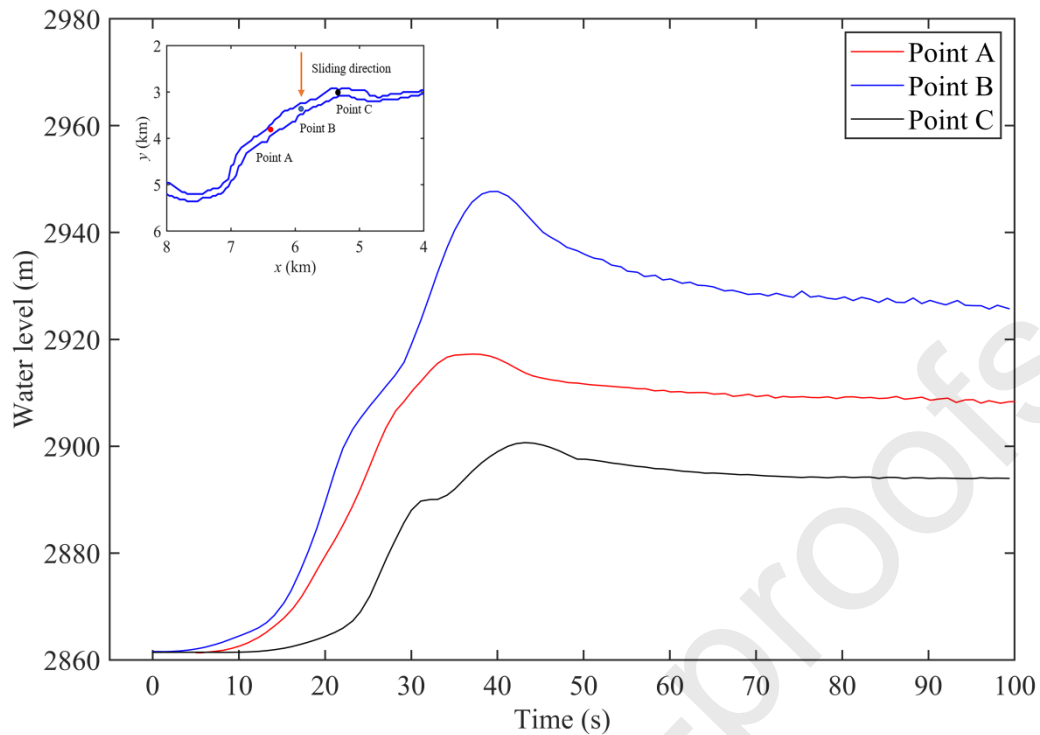
Fig. 5. Phase I "10.10" Baige landslide-generated waves: predicted water level hydrographs at three locations in the Jinsha river near Baige, Sichuan, China.

4.1.2. Landslide dam and barrier lake formation

Fig. 6(a) displays the landslide dam morphology, represented by deformation of the original bed, at $t = 900$ s. In general, the dam body is higher at the left bank than at the right bank. The landslide dam body is divided into four longitudinal sections (I, II, III, and IV) in the river flow direction, following Cai et al. (2019). Table 2 shows the consistent agreement obtained between the computed and measured elevations above sea level and lengths of the four longitudinal sections. Fig. 6(b) presents the predicted cross-section thickness profile at A-A' (Fig. 6a) of the landslide dam along the river, along with measured data from Fan et al. (2020a). Although discrepancies are appreciable between the present modelling and observed

21

data, the landslide dam morphology predicted by the present model is in good overall agreement with the measured data. In particular, the computed maximum dam height is 84.2 m, slightly higher than the measured value of 81.4 m. Quantitatively, the value of the L^1 norm for bed deposition thickness $L_{bd}^1 = 12.45\%$
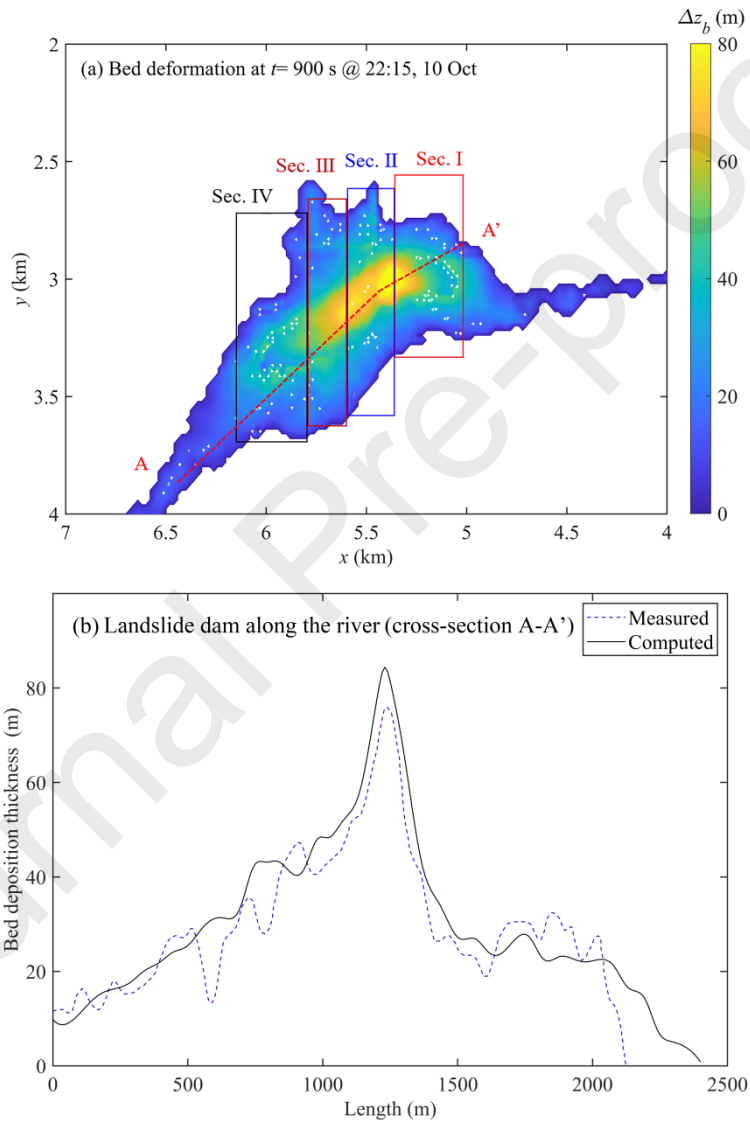

Fig. 6. "10.10" Baige landslide dam geometry: (a) bed deformation at $t = 900$ s predicted by present model; and (b) cross-section profile of landslide dam in the original river stream-wise direction (A-A'): model prediction (solid line) and measured data from Fan et al. (2020a) (dashed line).

Table 2 Summary of "10.10" Baige landslide dam morphology

Section	Elevation (m)		Length (m)	
	Computed	Measured[*]	Computed	Measured[*]
I	2996~3012	2998~3005	410	412
II	2965~2978	2973~2977	220	206
III	2963~2981	2977	250	215
IV	2943~2953	2948~2951	450	421

[*] Observed data from Cai et al. (2019)

Fig. 7 shows the landslide dam and barrier lake formation process due to the "10.10" Baige landslide impacting the Jinsha river as the water layer depth h_w, landslide layer thickness h_s, and bed deformation Δz_b evolve with time. The landslide first accelerates down the hillslope ramp (Figs. 7 a1-a2, b1-b2), then directly crashing into the river, and forcing the water to run up the opposite bank while generating large water waves (Figs. 7 a3, b3 and c3). Later, most of the landslide material is rapidly deposited on the riverbed, forming a landslide dam (Figs. 7 a4, b4 and c4). Meanwhile, water waves significantly erode the opposite riverbank (Fig. 7 c4), entraining more sediment into the river and further facilitating landslide dam formation. Soon after the landslide dam forms, a barrier lake is created due to the river blockage, and the volume of this lake gradually increases thereafter due to the sustained upstream inflow, as shown in Figs. 7(a5 and a6). During this stage, waves propagate back and forth upstream of the dam, affected by a combination of the sustained river inflow and the sudden arrival of the dam. By contrast, waves downstream of the landslide dam exhibit one-way propagation downstream adding to riverbed erosion.
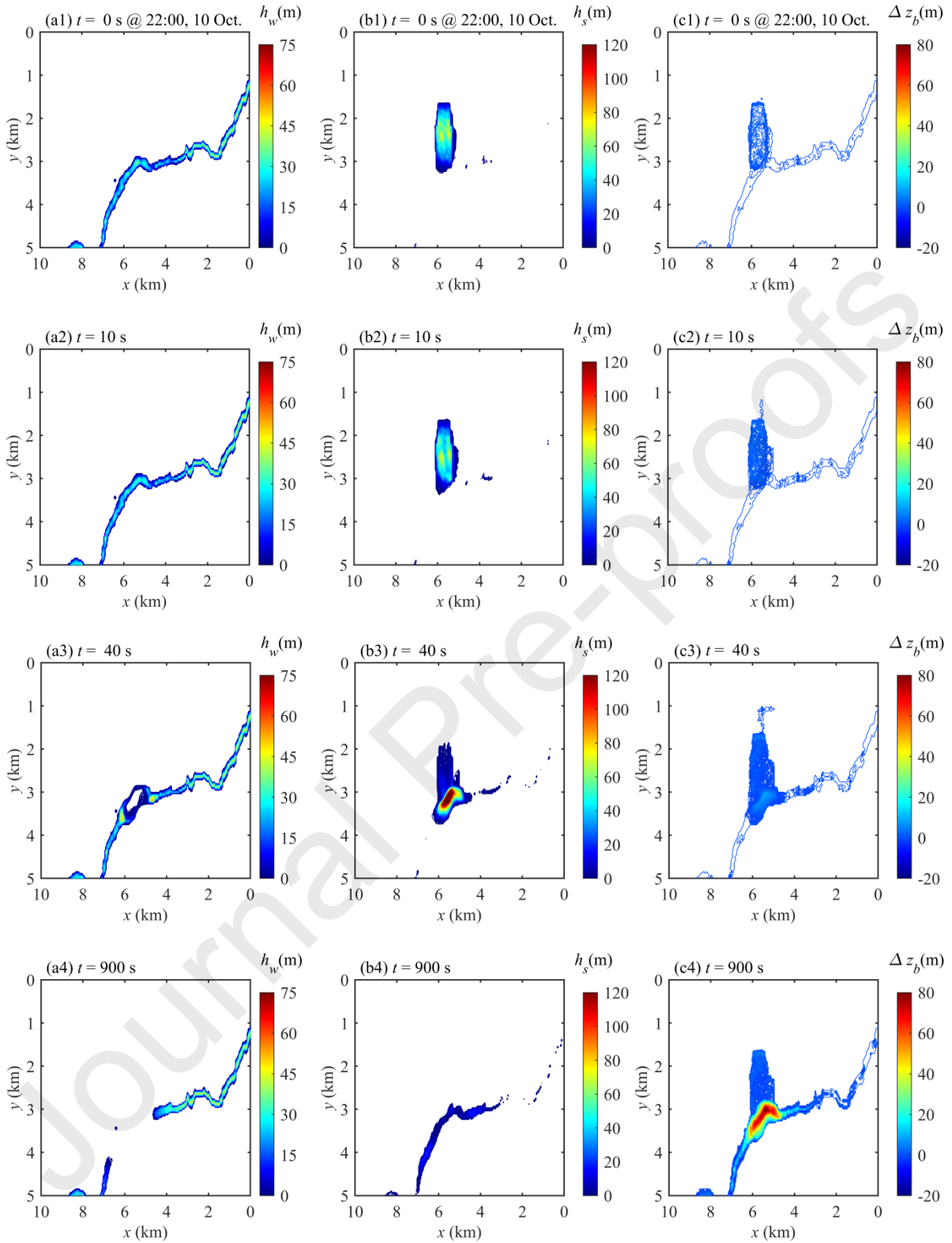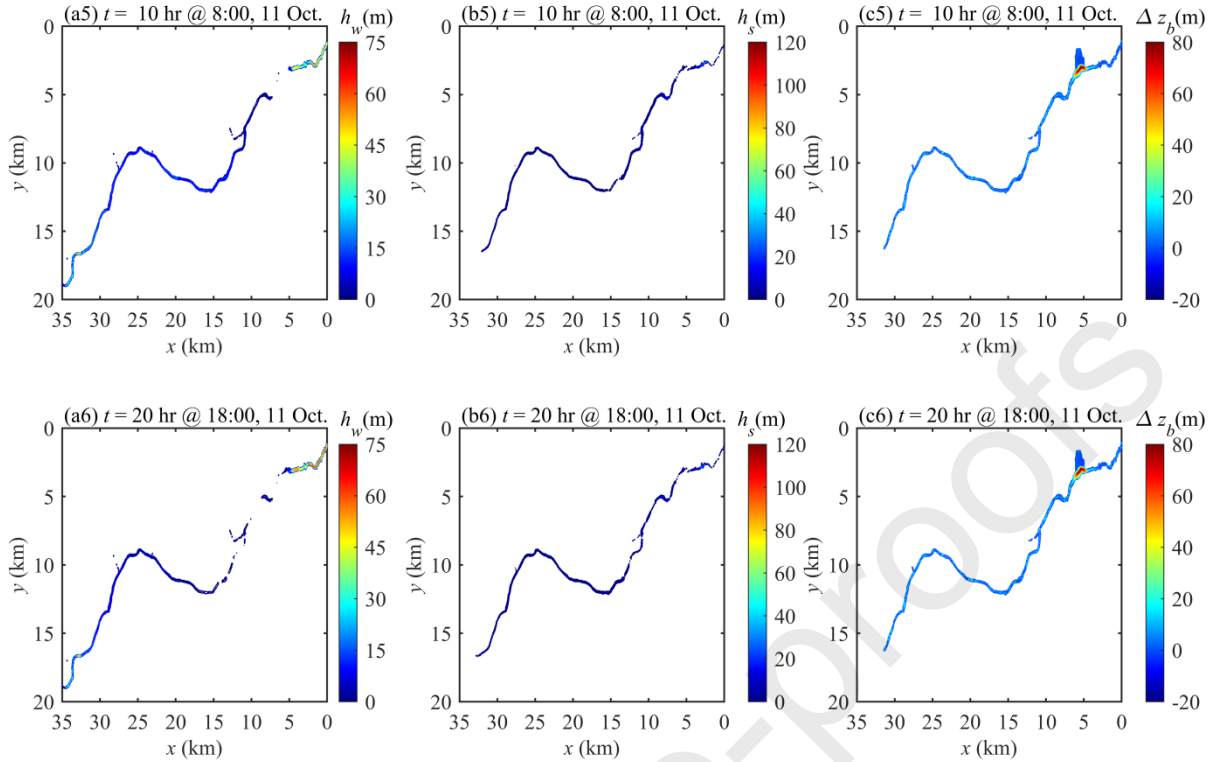
Fig. 7. "10.10" Baige landslide dam and barrier lake formation: (a1-a6) depth of water layer; (b1-b6) landslide thickness; and (c1-c6) bed deformation.

4.1.3. Barrier lake outburst and the resultant flood

The "10.10" Baige landslide dam was overtopped naturally at 17:30, 12 October. This overtopping flow increased drastically at midnight (00:00, 13 October), reached a peak value of approximately 10,000 m³/s at about 06:00 on 13 October, and returned to base flow at 14:30 on 13 October. Fig. 8(a) shows the excellent agreement obtained between the predicted breach flow hydrograph with the observed data reported by Cai et al. (2019). The predicted peak discharge of 9691 m³/s occurs at 05:45 on 13 October, and is slightly below the observed peak of 10,000 m³/s and 15 mins earlier than the observed time (06:00 on 13 October). The present model offers improved accuracy over simplified physically-based models (such as that of L. Zhang et al., 2019). Fig. 8(b) presents computed and measured

discharge hydrographs at the downstream gauging station at Yebatan, along with computed sediment volume output time series. Again, the model predictions closely match the measured data. It can be seen that the peak discharge is attenuated along the river. At Yebatan, the predicted peak discharge is 7941 m^3/s at 8:12 on 13 October, whereas the observed maximum discharge is 7822 m^3/s at 8:40 on 13 October. Thereafter, the discharge gradually reduces to base flow. By the end of "10.10" Baige barrier lake event, it is estimated that $3.48 \times 10^6\,m^3$ of sediments have been flushed downstream due to the outburst flood, thus the bulk aggradation in the river course between Baige dam site and Yebatan amounts to 2.4 $\times 10^7\ m^3$ [= $2.75 \times 10^7\ m^3$ (total volume of "10.10" Baige landslide) $-$ $3.48 \times 10^6\ m^3$ (sediment volume output)]. The L^1 norms for breaching flow discharge hydrograph $L^1_{Q_b}$ and flow discharge hydrograph at Yebatan gauging station L^1_Q are respectively 15.3% and 16.25%.

Fig. 9 presents the simulated time series of water levels at the barrier lake and several sites downstream of the landslide dam. Due to bursting of the barrier lake, its water level, indicated by the dashed line, decreases by over 27 m, which is consistent with the observed value in excess of 20 m reported by media. Water levels at locations downstream of the landslide dam site generally experience a sharp increase due to the arrival of the outburst flood and then a relatively flatter decrease with time. Similar to the peak discharge (Fig. 8), the amplitude of water level rise becomes increasingly attenuated with distance along the river (the value decreases from 28 m at a location 5 km downstream of the dam to 13.5 m at Yebatan).
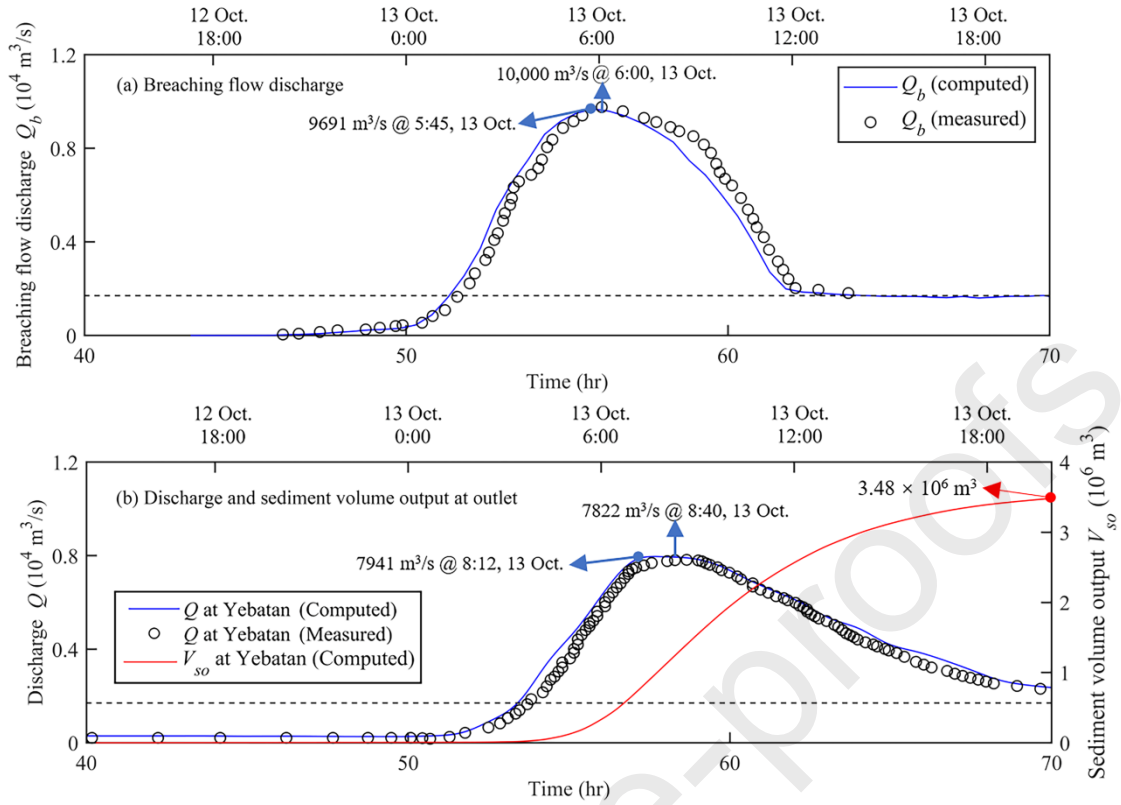
Fig. 8. (a) Breaching flow discharge hydrograph and (b) flow discharge hydrograph and sediment volume output time series at the Yabatan gauging station: model predictions (solid lines) and measured data from Cai et al. (2019) (open black circles).
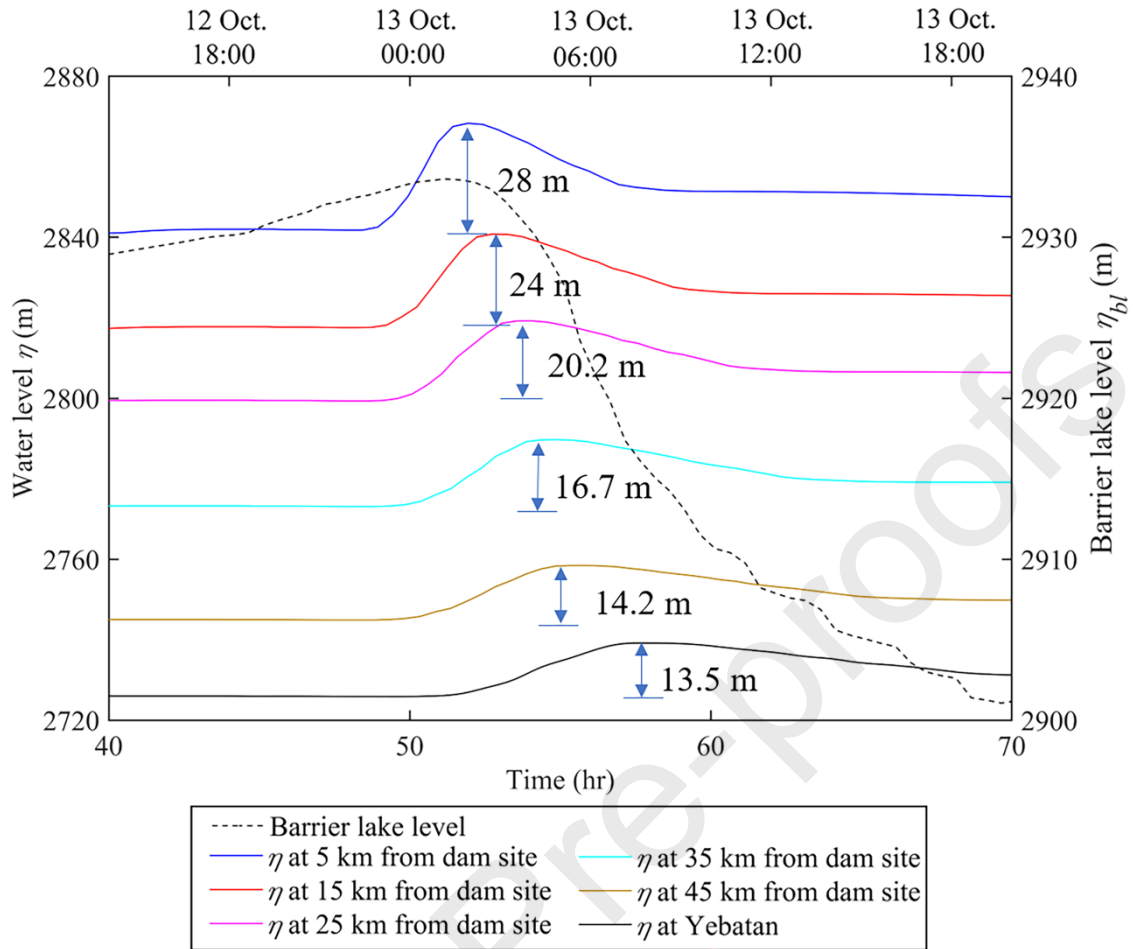
Fig. 9. Water level time series at the barrier lake and selected sites downstream of the "10.10" Baige landslide dam.

Fig. 10 presents contour plots of the water depth, sediment layer thickness, and changes to bed elevation at different times throughout the barrier lake outburst and subsequent flood processes. Once the barrier lake fills with upstream river inflow, the lake's water level exceeds the crest of the dam and overtopping begins (Fig. 10a1, $t =$ 43 hr at 17: 00 on 12 October), and the landslide dam body is slightly eroded (Fig. 10c1). The predicted time of first overtopping is half-hour earlier than measured. Five hours after overtopping commences ($t =$ 48 hr at 22: 00 on 12 October), the breaching flow reaches Yebatan and the Jinsha river

downstream of the landslide dam resumes flowing with a rather low discharge (Fig. 10a2).

Meanwhile, the overtopping flow gradually erodes the downstream face of the landslide dam

(Fig. 10c2). Subsequently, the overtopping flow rapidly increases (Fig. 8), attaining a value

almost equal to the upstream inflow discharge by $t = $ 51 hr at 01: 00 on 13 October and

peaking at $t = $ 55.75 hr at 05: 45 on 13 October. During this stage, the water depth

downstream of the landslide dam significantly increases, while its upstream counterpart

accordingly decreases (Fig. 10(a3-a4)). Within a further two and half hours, the peak

discharge arrives at Yebatan (Fig. 10a5). Meanwhile the landslide dam is eroded remarkably,

leading to a significant decrease in its crest elevation (Fig. 10(c3-c5)). After time $t = $ 64 hr at

14: 00 on 13 October, a new river channel forms and the Jinsha river resumes base flow, and

is unable to erode further the landslide dam, thus terminating the dam breach process (Fig.
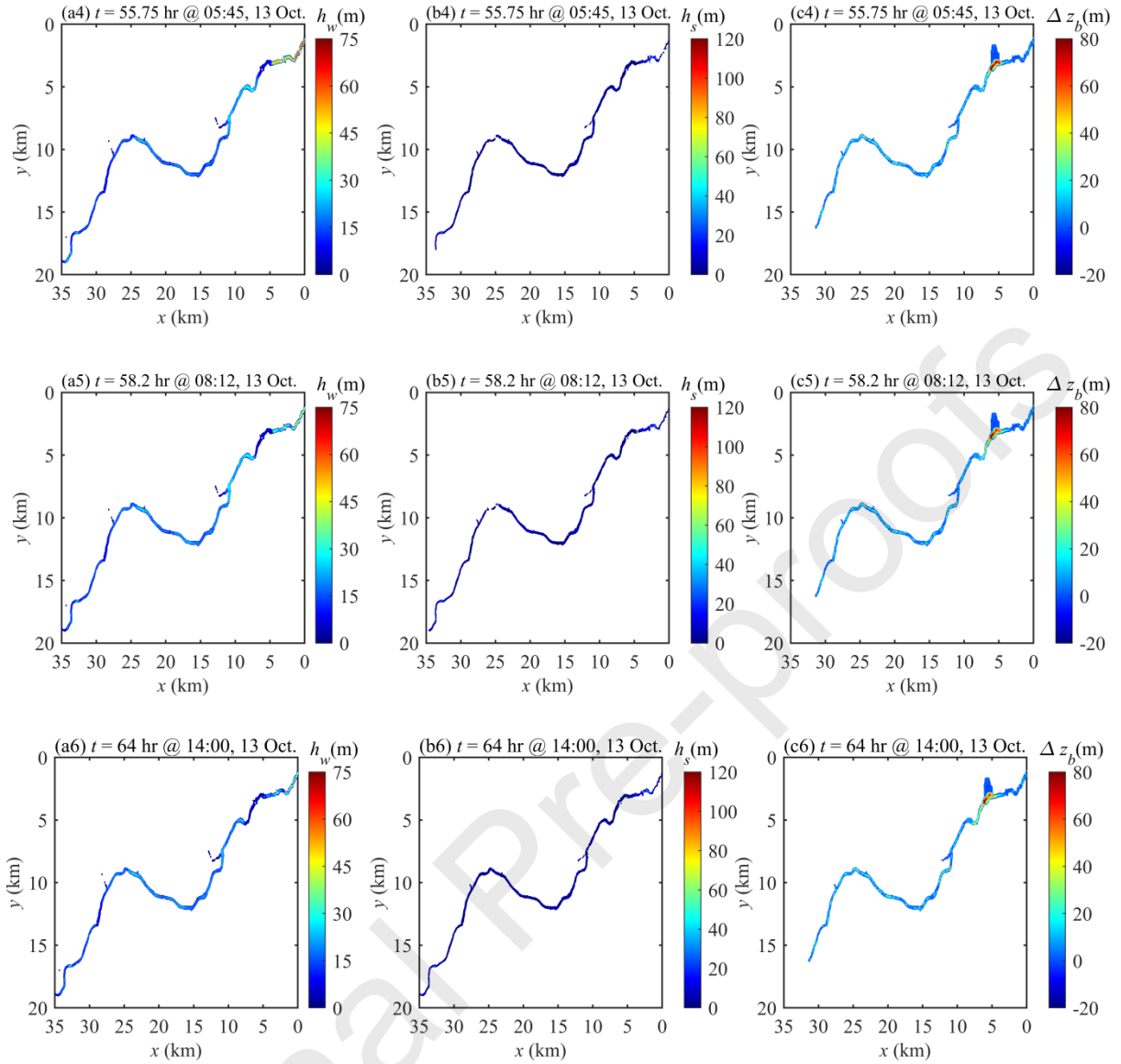
10(a6, b6 and c6)).
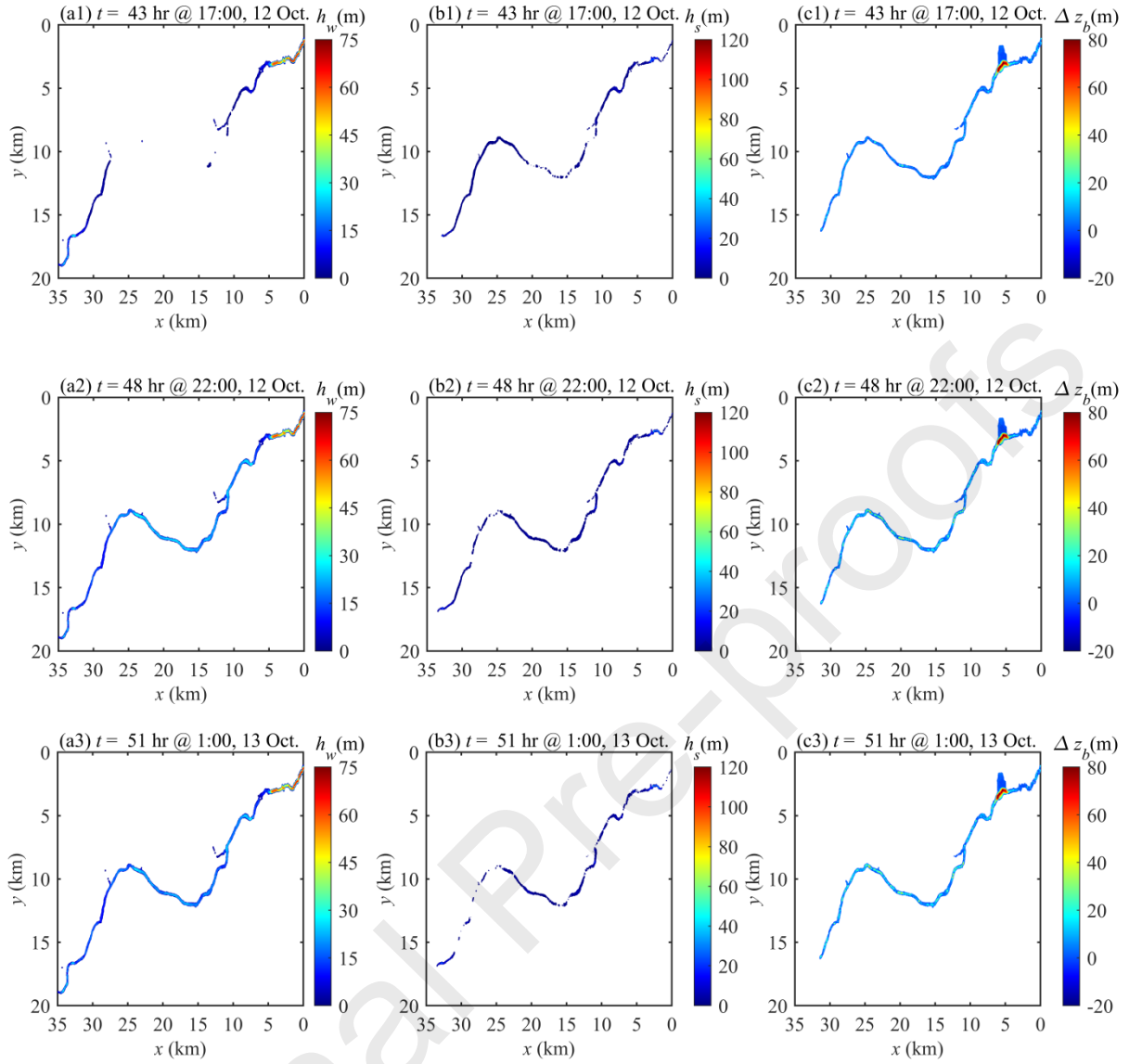
Fig. 10. "10.10" Landslide-induced barrier lake outburst and the resultant flood: (a1-a6) depth of water layer; (b1-b6) water-sediment mixture thickness; and (c1-c6) bed deformation. (a1, b1 and c1) Landslide dam is overtopped naturally and dam breach commences. (a2, b2 and c2) Breaching flow arrives at Yebatan. (a3, b3 and c3) Breaching flow discharge is almost equivalent to upstream inflow discharge. (a4, b4 and c4) Breaching flow peaks. (a5, b5 and c5) Peak breaching flow arrives at Yebatan. (a6, b6 and c6) Jinsha river resumes its base flow and the dam breach process terminates.

4.1.4 Interphase interactions

Interphase interactions are evaluated by means of relative velocities. Physically, interphase interactions quantify momentum and energy transfers between grains and fluid (Shan and Zhao, 2014), and hence characterize wave hydrodynamics and sediment transport arising from granular landslides impacting water bodies (Zitti et al., 2016; Miller et al., 2017). Based on laboratory-scale case studies, Li et al. (2020) revealed that grains play a key role in driving water movement during the formation of a landslide dam and its associated barrier lake. However, the subsequent dam breaching process has not yet been fully resolved. Here U_{fs} and V_{fs} are defined as longitudinal (x–axis) and transverse (y–axis) velocity differences between the water phase of the water-sediment mixture flow layer and the sediment phase of a given size Accordingly, $U_{fs}=u_f - u_{sk}$ and $V_{fs}=v_f - v_{sk}$, where u_f and v_f are the layer-averaged velocity components of the water phase in the water-sediment mixture flow layer; and u_{sk} and v_{sk} are the size-specific layer-averaged velocity components of the sediment phase in the water-sediment mixture flow layer. Fig. 11 displays the velocity differences between the water and size-specific sediment phases in the transverse direction, and Fig. 12 shows their counterparts in the longitudinal direction. Specifically, Figs. 11 (a1-a3 and b1-b3) and Fig. 12 (a1-a3 and b1-b3) depict the barrier lake formation process, whereas the remaining subplots refer to the barrier lake outburst and subsequent flood.

During barrier lake formation, as seen in Figs. 11 (a1-a3 and b1-b3) and Figs. 12 (a1-a3 and b1-b3), sediment grains play a primary role in driving water movement, echoing the finding from a laboratory-scale study by Li et al. (2020). Specifically, the grains generally

have higher speed than the water phase in both the transverse and longitudinal directions. Comparatively, the magnitude of velocity difference in the transverse direction (V_{fs}) is significantly greater than that in the longitudinal direction (U_{fs}). Furthermore, coarse grains move approximately 30% - 40% faster than fine grains in the transverse direction (Fig. 11(a1-a2)), whereas the velocity difference shrinks to 10%-20% in the longitudinal direction (Fig. 12(a1-a2)). By $t = $ 900 s, as a landslide dam forms due to material deposition, the velocity differences between the water and sediment phases almost vanish.

By contrast, the reverse behaviour occurs during the succeeding processes, as water governs grain movement. Figs. 11 (a4-a5 and b4-b5) and Figs. 12 (a4-a5 and b4-b5) show that the water phase generally exhibits higher speed than the grains, and that fine grains move faster than coarse grains. Although measured data are unavailable to verify quantitatively the computed results, the present finding is qualitatively consistent with existing experimental fluvial process observations (Wilcock, 1997) and field data (Drake et al., 1988; Ferguson and Wathen, 1998; Lenzi, 2004); this further demonstrates the satisfactory performance of the present model.

Figs. 11 and 12 collectively show that water and grain velocities are distinct, thus characterizing the primary role of grains in driving water movement during landslide dam and barrier lake formation and the governing role of water in driving grain movement during barrier lake outburst and the subsequent flood. Overall, these results imply that a double layer-averaged two-phase flow model is warranted.
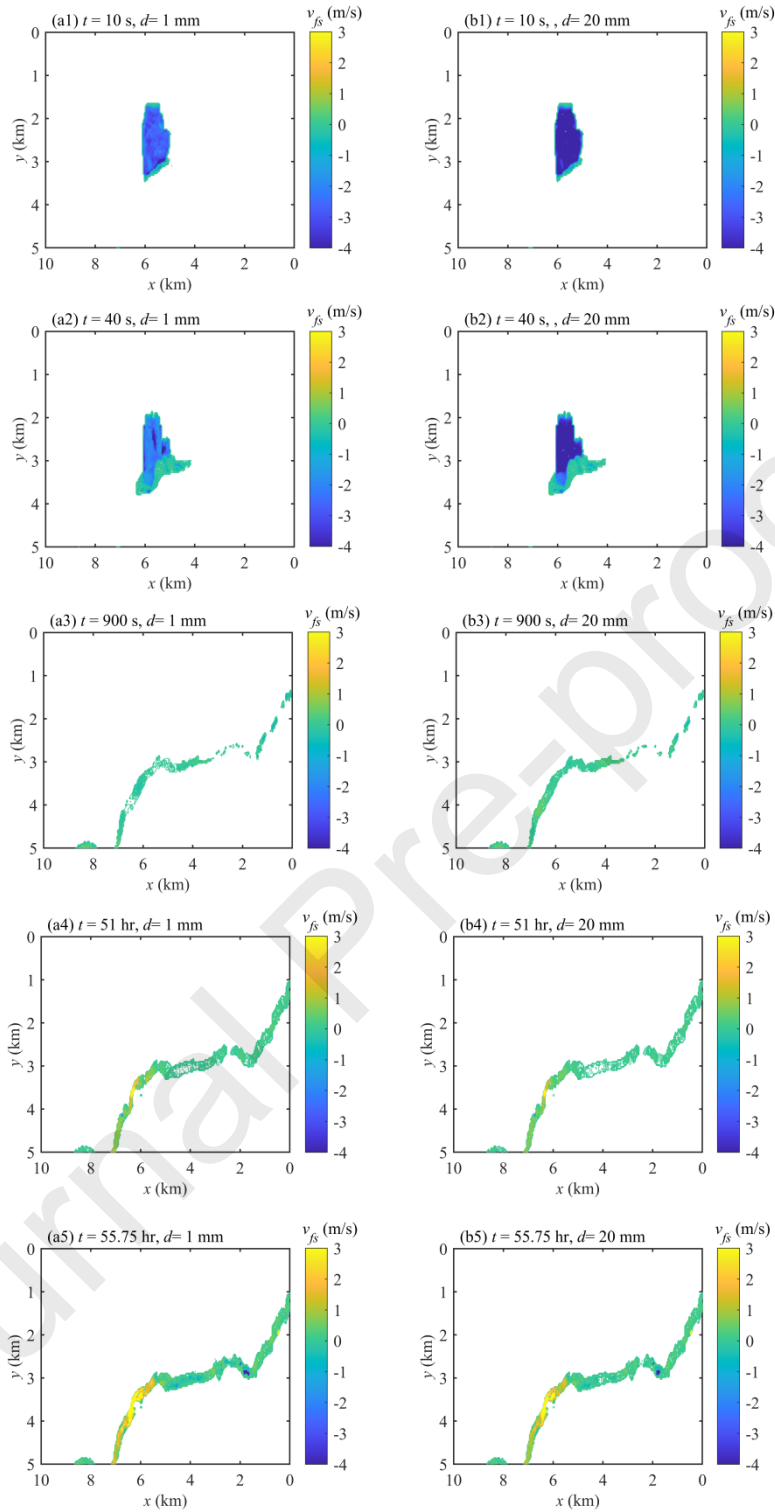
Fig. 11. Contour plots of velocity difference between water and sediment phases of the water-sediment mixture flow layer in the transverse (y – axis) direction at different times from 10 s to 55.75 hr after the start of the "10.10" Baige landslide: a1–a5 with $d = 1$ mm; and b1–b5 with $d = 20$ mm.
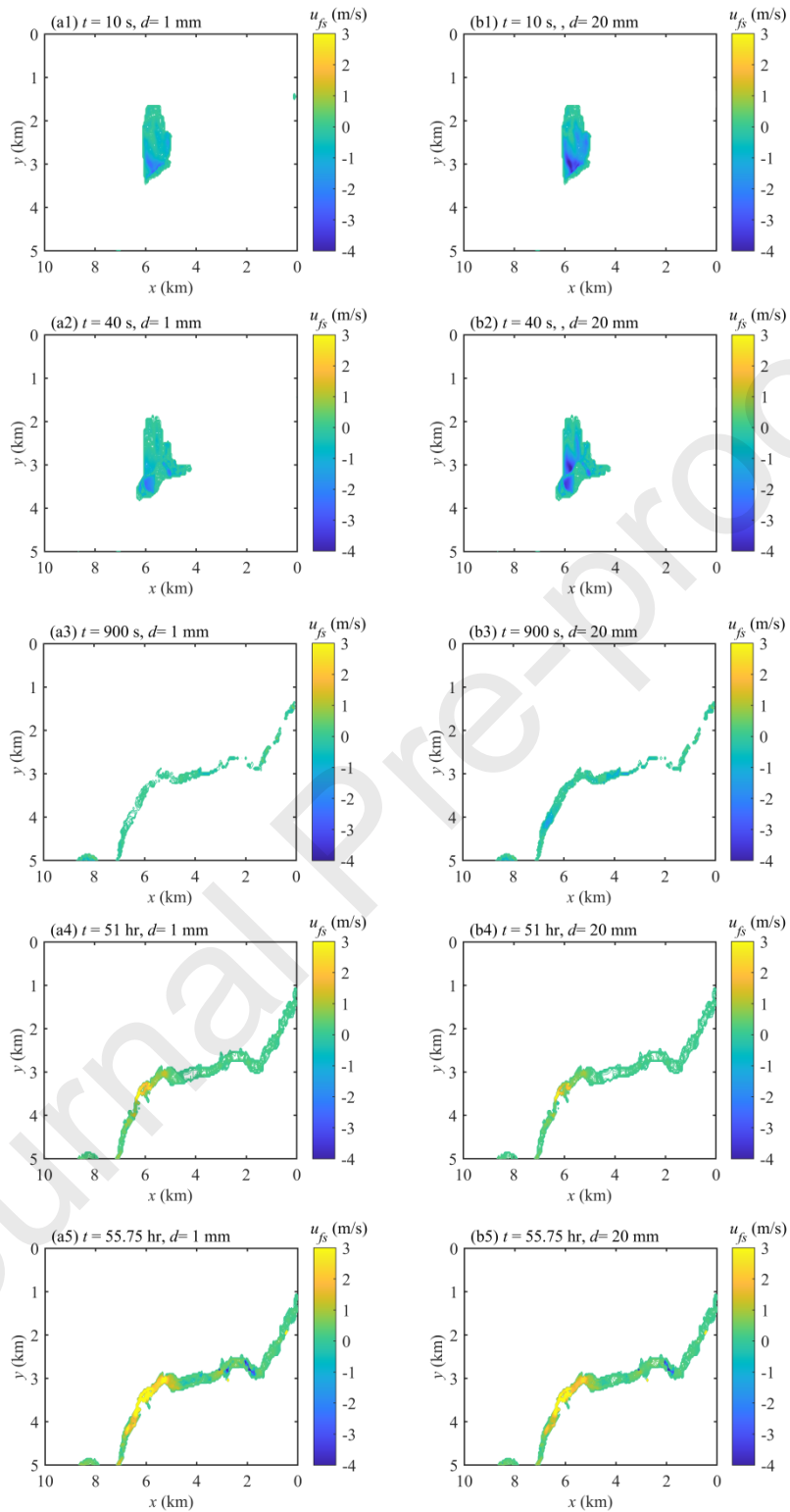
Fig. 12. Contour plots of velocity difference between water and sediment phases of the water-sediment mixture flow layer in the longitudinal (x – axis) direction at different times from 10 s to 55.75 hr after the start of the "10.10" Baige landslide, a1-a5 with $d = $ 1 mm,

and b1-b5 with $d = 20$ mm.

4.1.5. Effects of inflow discharge and landslide volume

Laboratory-scale case studies have found that smaller river flow discharge and larger landslide volume favour landslide dam and barrier lake formation (Li et al., 2020). Here, two series of extended numerical cases, designed according to the Phase I "10.10" Baige barrier lake event, are used to investigate the effects of inflow discharge and landslide volume on a landslide-induced multi-hazard chain. This is sensible given that potentially unstable rock mass clusters have been discovered in the source area of the Baige landslides, suggesting possible future failures with the potential for river damming and flooding (Fan et al. 2020a).

4.1.5.1. Inflow discharge (Series 1 tests)

Runoff variations in the upper tributaries of the Jinsha River are vulnerable to climate change (Wu et al., 2020). It is therefore useful to explore the impacts of different upstream inflow discharges on the landslide-induced multi-hazard chain. Here, the inflow discharge is tuned by 25% (i.e., 1680 ± 420 m³/s), and the corresponding results are displayed in Table 3 and Fig. 13. As the inflow discharge increases, the time taken to form a landslide dam increases and the dam height decreases. This is consistent with the observation by Li et al. (2020) that small river discharge is conducive to barrier lake formation. In the present simulations, the time taken to overtop the dam drops substantially from 50.3 hr to 43 hr, and further to 36.5 hr, as the inflow discharge increases from 1260 m³/s to 1680 m³/s, and further to 2100 m³/s. From these, corresponding marked reductions in the time available to evacuate downstream residents may be inferred. Therefore, the risk arising from a barrier lake outburst

36

would be significantly amplified if the barrier lake was created in the rainy season. The simulations also indicate that after the dam overtops naturally, the subsequent peak breach flow discharge increases for higher inflow discharge (Table 3 and Fig. 13). Consequently, the larger the inflow discharge, the more rapidly the dam is eroded and the shorter the total breach duration.

Table 3 Predicted effect of inflow discharge on landslide dam formation, overtopping, and breaching processes (Series 1 tests)

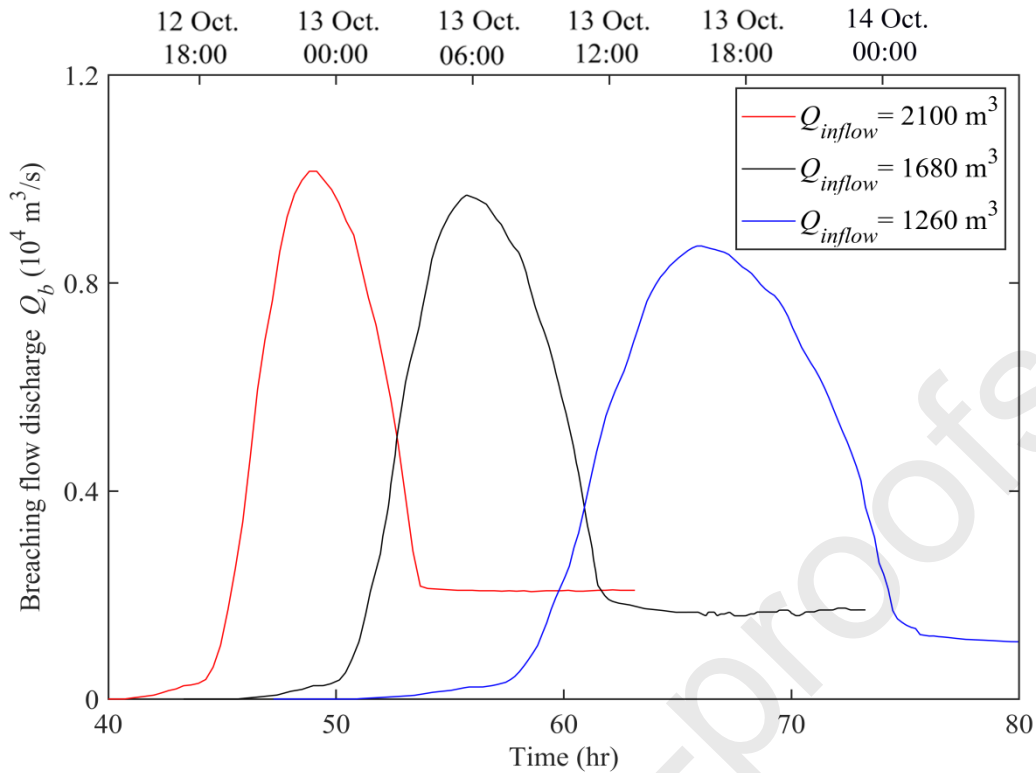| Results	"10.10" Baige landslide	Series 1-1	Series 1-2
	Q_{inflow} (m³/s)	Q_{inflow} (m³/s)	Q_{inflow} (m³/s)
	1680	2100	1260
Time to form landslide dam (s)	900	1230	765
Maximum dam height (m)	84.2	76.5	87.2
Time to overtop dam (hr)	43	36.5	50.2
Total breach duration (hr)	21	18.5	23
Peak discharge at dam site (m³/s)	9691	10006	8724

Fig. 13. Model predictions of breaching flow discharge hydrographs for three different Jinsha river inflow discharges.

4.1.5.2. Initial landslide volume (Series 2 tests)

For landslide-induced risk assessment, it is of great importance to obtain a measure of the landslide magnitude, e.g., through estimating the volume of landslide materials involved (Corominas et al., 2014; Fan et al., 2020b). Although the position and movement of a landslide can be successfully captured by advanced techniques like remote sensing (Zhang et al., 2020), quantification of the initial volume of a landslide nevertheless involves considerable uncertainty. With this in mind, Series 2 simulations have been undertaken to investigate the sensitivity of the results to the initial landslide volume, which is altered by $\pm 50\%$ of the original volume of $27.5 \times 10^6 \, \text{m}^3$. Table 4 summarizes the results from the Series 2 simulations, whereas Fig. 14 displays the breaching flow hydrograph under different initial

landslide volumes. In accordance with Li et al. (2020), a larger initial landslide volume favours barrier lake formation as the time to form a landslide dam decreases and the maximum dam height increases. Hence, the time taken to overtop the dam increases as the initial landslide volume increases. Subsequently, the breaching process is postponed and the total breach duration extended. Yet, the peak discharge at the dam site just slightly increases.

Table 4 Predicted effect of inflow landslide volume on landslide dam formation, overtopping, and breaching processes (Series 2 tests)

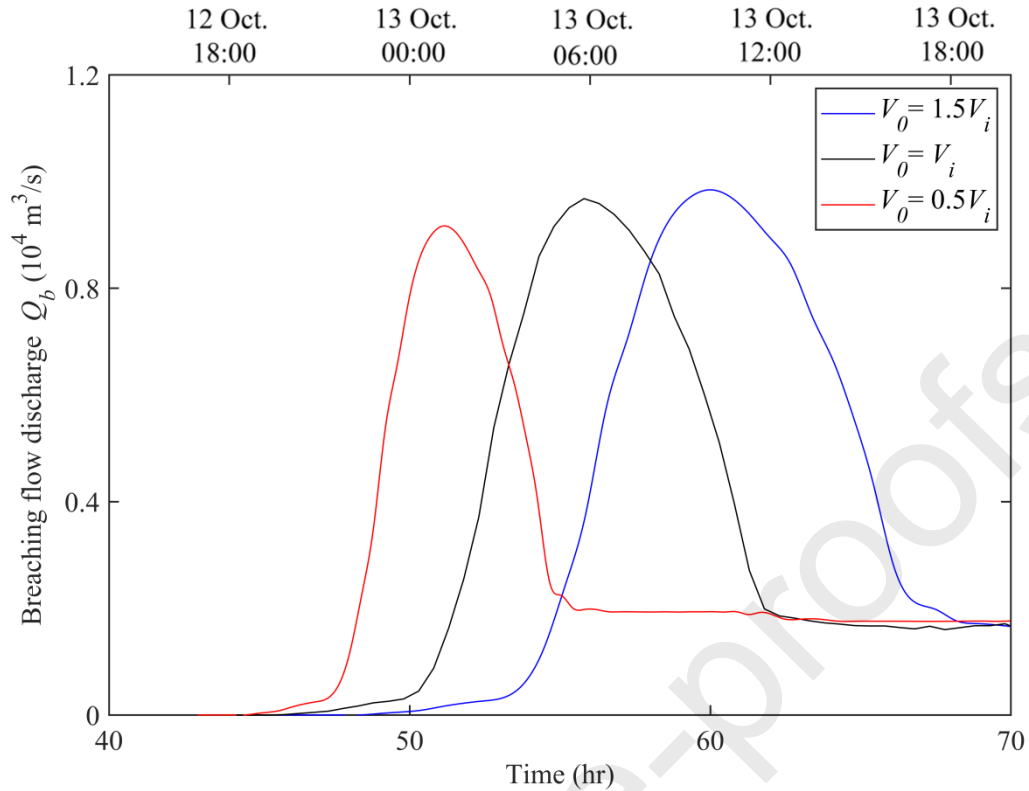| Results	"10.10" Baige landslide	Series 2-1	Series 2-2
	V_0	V_0	V_0
	(10^6 m^3)	(10^6 m^3)	(10^6 m^3)
	27.5	41.25	13.75
Time to form landslide dam (s)	900	700	1356
Maximum dam height (m)	84.2	90.2	74.5
Time to overtop dam (hr)	43	45.3	40.5
Total breach duration (hr)	21	23.7	16.5
Peak discharge at dam site (m³/s)	9691	9845	9170

39

Fig. 14. Model predictions of breaching flow discharge hydrographs for three different initial landslide volumes.

The above analysis clearly demonstrates that whereas small inflow discharge and large initial landslide volume favour landslide dam and barrier lake formation, they delay the subsequent barrier lake outburst and the resultant flood downstream. From a physical perspective, the formation of a landslide dam and its associated barrier lake generally reflects an aggradation process, whereas the barrier lake outburst and subsequent flood are characterized by an opposing degradation process. The present model properly accommodates these two distinct but intertwined physical processes, thus facilitating improved understanding of the complicated physical mechanisms leading to a landslide-induced barrier lake outburst flood as a multi-hazard causal chain.

4.1.6 Sensitivity analysis

Furthermore, numerical tests are conducted to evaluate the sensitivity of the model results to two model parameters, i.e., bed friction coefficient $\tan\delta$ and Manning bed roughness coefficient n_b, which are separately embedded in the empirical relationships for the solid and fluid resistance components of the lower sediment-laden flow layer. In addition, the Manning bed roughness coefficient n_b is also involved in the bottom resistance of the clear-water flow layer (Li et al., 2020). Specifically, the Manning bed roughness coefficient n_b and the bed friction coefficient $\tan\delta$ are tuned by 25% of the adopted value (i.e., $n_b = 0.04 \pm 0.01$ m$^{-1/3}$ s; $\tan\delta = 0.7 \pm 0.14$). In general, the results with tuned parameters in conventional ranges are qualitatively similar to those shown above when compared with the measured data.

Shown in Figs. 15 and 16 are the computed landslide dam morphology, corresponding to different values of n_b and $\tan\delta$. Clearly, the computed results are more sensitive to the value of bed friction coefficient $\tan\delta$ as compared to that of Manning bed roughness coefficient n_b. Most notably, the sensitivity to n_b is considerably constrained compared with that to $\tan\delta$. Typically, as the value of $\tan\delta$ increase from 0.56 to 0.84, the value of maximum dam height increases from 59.2 m to 89.5 m. By contrast, in response to the change of n_b, their counterparts almost remain unchanged. This difference in behavior further demonstrates the primary role of grains in driving water movement during landslide dam and barrier lake formation.

41

Fig. 17(a) shows the impact of $\tan\delta$ on breaching flow discharge. As shown in Fig. 15, a larger value of $\tan\delta$ leads to a higher maximum dam height. Consequently, the time taken to overtop the dam increases and the subsequent breaching process is postponed. These simulations also indicate that the peak breaching flow discharge increases for a larger value of $\tan\delta$. Specifically, with $\tan\delta = 0.56$, the peak discharge is 8732 m³/s occurring at $t =$ 49.6 hr, whereas with $\tan\delta = 0.84$, the peak discharge increases to 10170 m³/s, postponing to $t = $ 61.88 hr. Fig. 17(b) illustrates the effect of n_b. Despite its marginal impact on landslide dam morphology, a larger value of n_b leads to a larger peak discharge and an earlier occurrence. Specifically, with n_b increasing from 0.03 to 0.05 m⁻¹ᐟ³ s, the peak discharge increases from 8700 m³/s to 10400 m³/s and its timing is advanced from $t = $ 61.3 hr to $t =$ 51.6 hr.
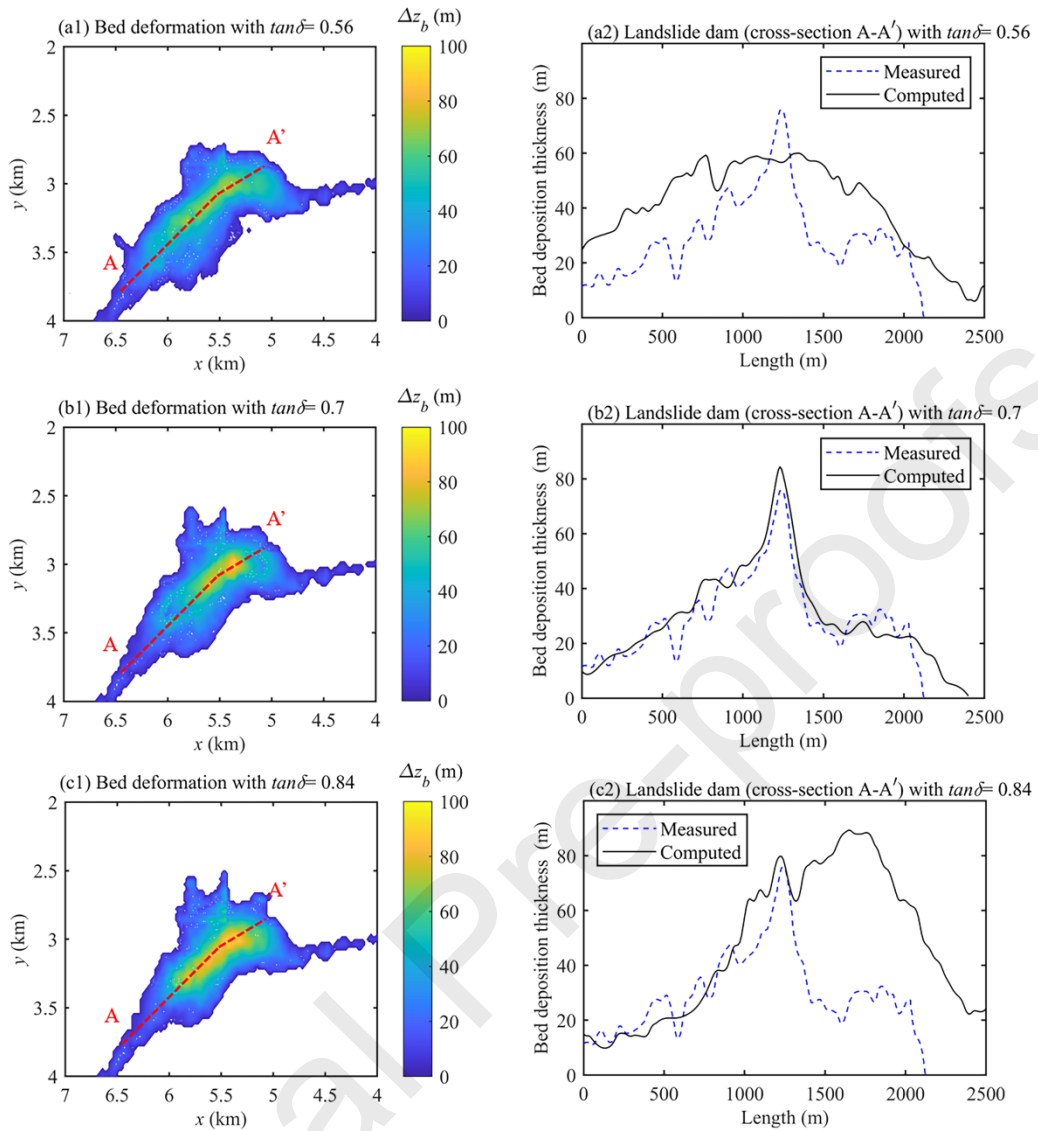
Fig. 15. "10.10" Baige landslide dam morphology assuming different bed friction coefficient $\tan\delta$ (a1-a3) bed deformation at $t = 900$ s predicted by present model; and (b1-b3) cross-section profile of landslide dam in the original river stream-wise direction (A-A'): model prediction (solid line) and measured data from Fan et al. (2020a) (dashed line).
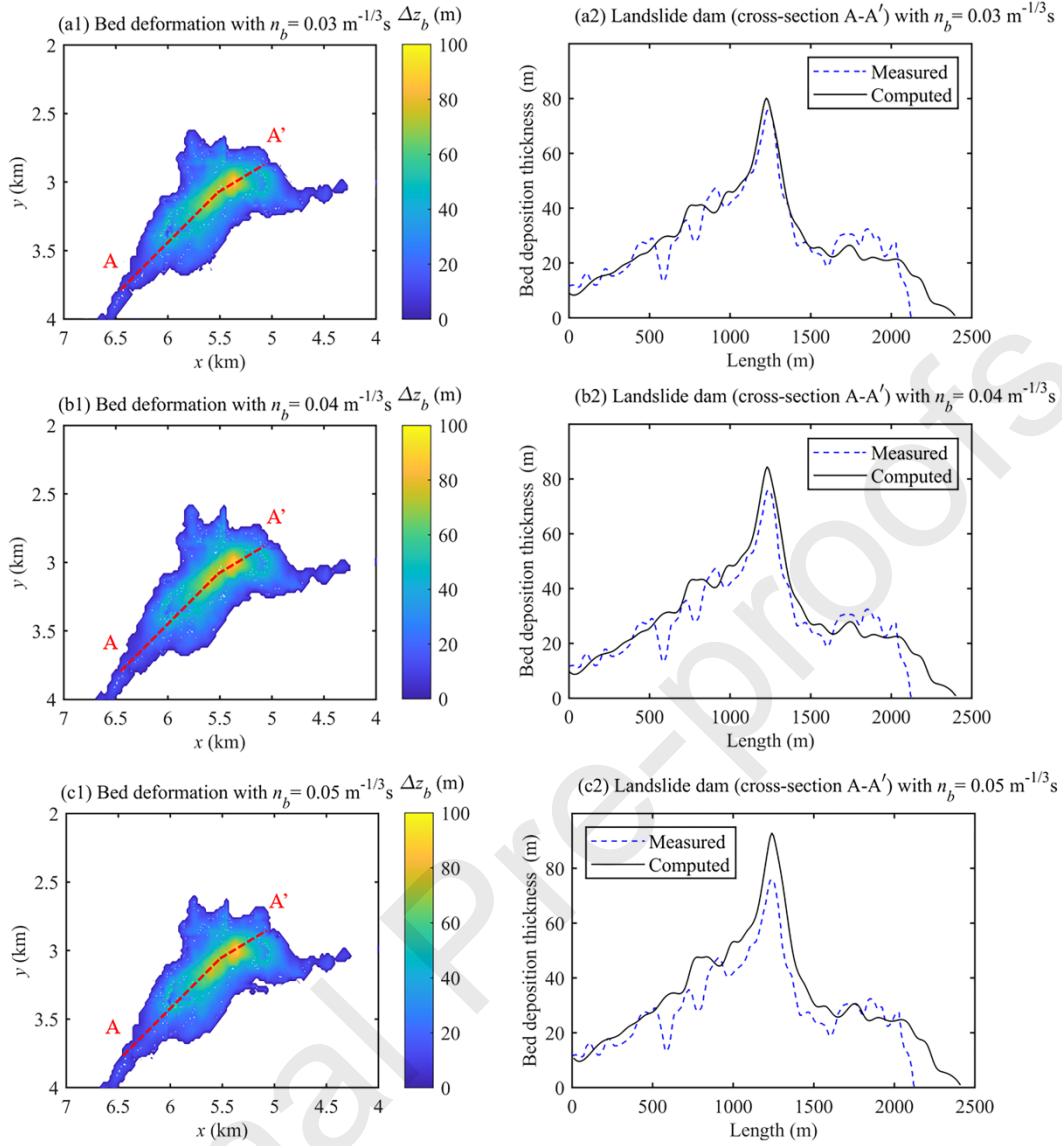
(a1) Bed deformation with $n_b = 0.03$ m$^{-1/3}$s Δz_b (m)

(a2) Landslide dam (cross-section A-A$'$) with $n_b = 0.03$ m$^{-1/3}$s

(b1) Bed deformation with $n_b = 0.04$ m$^{-1/3}$s Δz_b (m)

(b2) Landslide dam (cross-section A-A$'$) with $n_b = 0.04$ m$^{-1/3}$s

(c1) Bed deformation with $n_b = 0.05$ m$^{-1/3}$s Δz_b (m)

(c2) Landslide dam (cross-section A-A$'$) with $n_b = 0.05$ m$^{-1/3}$s

Fig. 16. "10.10" Baige landslide dam morphology assuming different Manning roughness coefficient n_b (a1-a3) bed deformation at $t = 900$ s predicted by present model; and (b1-b3) cross-section profile of landslide dam in the original river stream-wise direction (A-A'): model prediction (solid line) and measured data from Fan et al. (2020a) (dashed line).
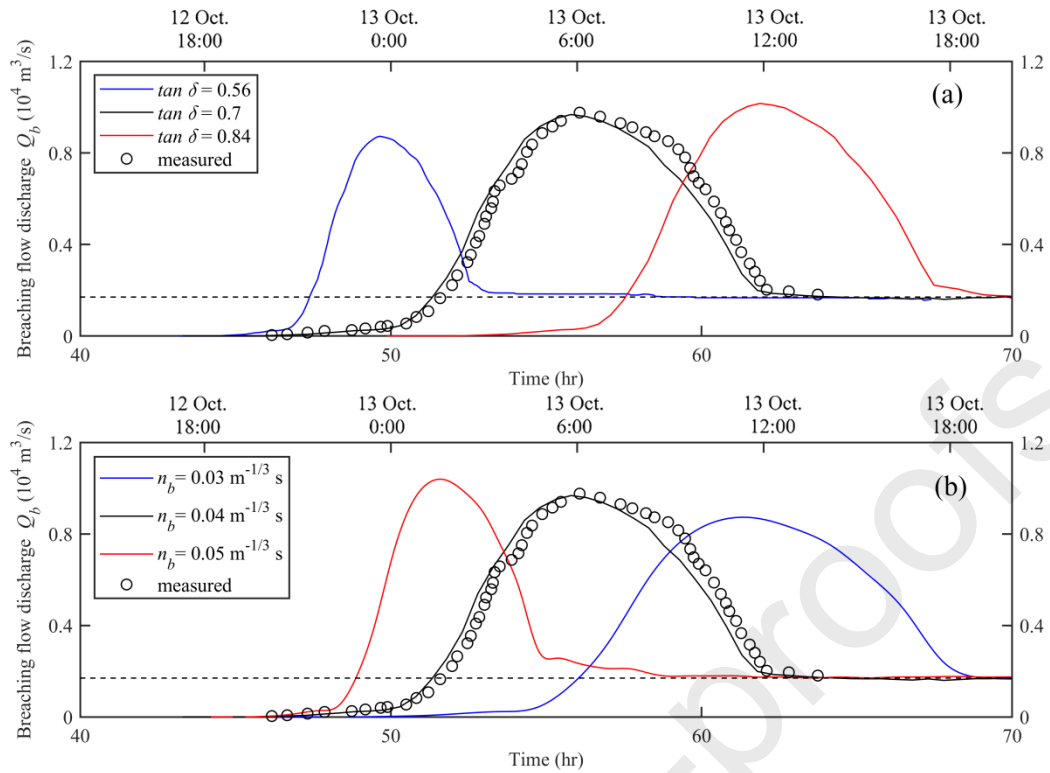
Fig. 17. Model predictions (solid lines) of breaching flow discharge hydrographs assuming (a) different bed friction coefficient $\tan\delta$; and (b) different Manning roughness coefficient n_b and measured data (open circles) from Cai et al. (2019).

4.2. Phase II: "11.03" Baige barrier lake event

We now revisit the Phase II "11.03" Baige barrier lake event. This second landslide dam formed on residual material from the first landslide dam, causing the barrier lake to triple in volume. To reduce downstream flood risk due to barrier lake outburst, an artificial flood channel was urgently constructed, with a total of 85,000 m³ of soil and rock excavated (Cai et al., 2019).

Fig. 18(a) shows the landslide dam morphology as represented by the bed deformation at $t = 900$ s (noting that $t = 0$ s is now set to the start of the "11.03" landslide). Similar to its predecessor due to the first landslide (Fig. 6), the height of the second landslide dam is higher on the upstream relative to the downstream side with respect to the Jinsha river. Fig. 18(b)

presents predicted and observed cross-section profiles of the landslide dam taken in a longitudinal direction approximately along the river (B-B', see Fig. 18a). The L^1 norm for bed deposition thickness L^1_{bd} = 22.38%. The present model predictions are in reasonable agreement with observed data, except for a general overprediction of the bed deposition layer thickness.

Fig. 19 presents discharge hydrographs and water level time series at the landslide dam site and the Yebatan station. Although quantitative differences between the model predictions and field observations are inevitable, the computed discharges and water levels are reasonably consistent with those reported by Cai et al. (2019). The model predicts a peak breach discharge of 32,787 m^3/s, occurring at 17:28 on 13 November, a difference in maximum discharge of 3.2% and occurrence time of < 1 hr compared to the observed data. The predicted water level time history at the dam site is remarkably close to the measured series at Boluo station, 20 km upstream of the dam, until the barrier lake outburst occurs, after which the predicted result at the dam site is appreciably lower than that measured at Boluo. This behaviour arises because the water level at the Baige landslide dam site was almost equivalent to that at Boluo while the barrier lake is full, but was appreciably lower than that at Boluo after the barrier lake outburst occurred. Fig. 19(b) compares predicted and measured discharge hydrographs at Yebatan, the downstream station, along with computed sediment volume output time series. Similar to the results obtained for Phase II (Fig. 8), the peak discharge attenuates as the wave travels along the river. At Yebatan, the peak discharge is predicted to occur at 19:10 on 13 November, with a value of 26,817 m^3/s, whereas the observed maximum discharge is 28,057 m^3/s at 19:50 on 13 November. Subsequently, the

Jinsha river gradually reverts to base flow. The corresponding L^1 norms for breaching flow discharge hydrography $L^1_{Q_b}$ and flow discharge hygrograph at Yebatan gauging station L^1_Q are 23.22% and 25.47% respectively. At the end of "11.03" Baige barrier lake event, approximately 5.96×10^6 m^3 of sediments have been carried away through Yebatan. Consequently, an addition 6.04×10^6 m^3 of sediment [$= 12 \times 10^6$ m^3 (total volume of "11.03" Baige landslide) $- 5.96 \times 10^6$ m^3 (sediment volume output)] has been deposited in the river channel between dam site and Yebatan.
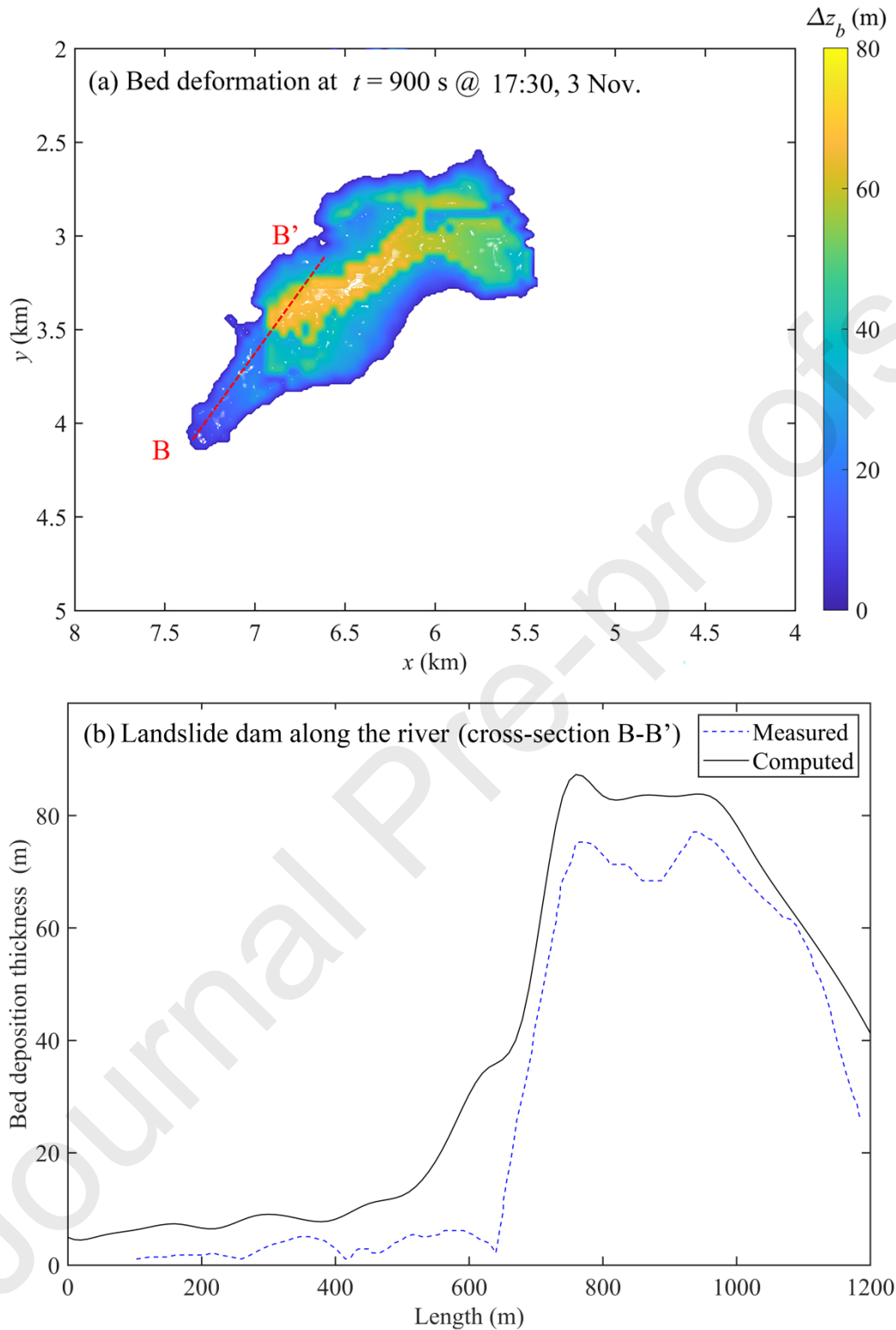
Fig. 18. "11.03" Baige landslide dam geometry: (a) predicted bed deformation contours at

$t =$ 900 s; and (b) predicted (solid line) and measured (dashed line, Fan et al. 2020a)

cross-sectional profiles of the landslide dam in a longitudinal direction along the river (B-B').
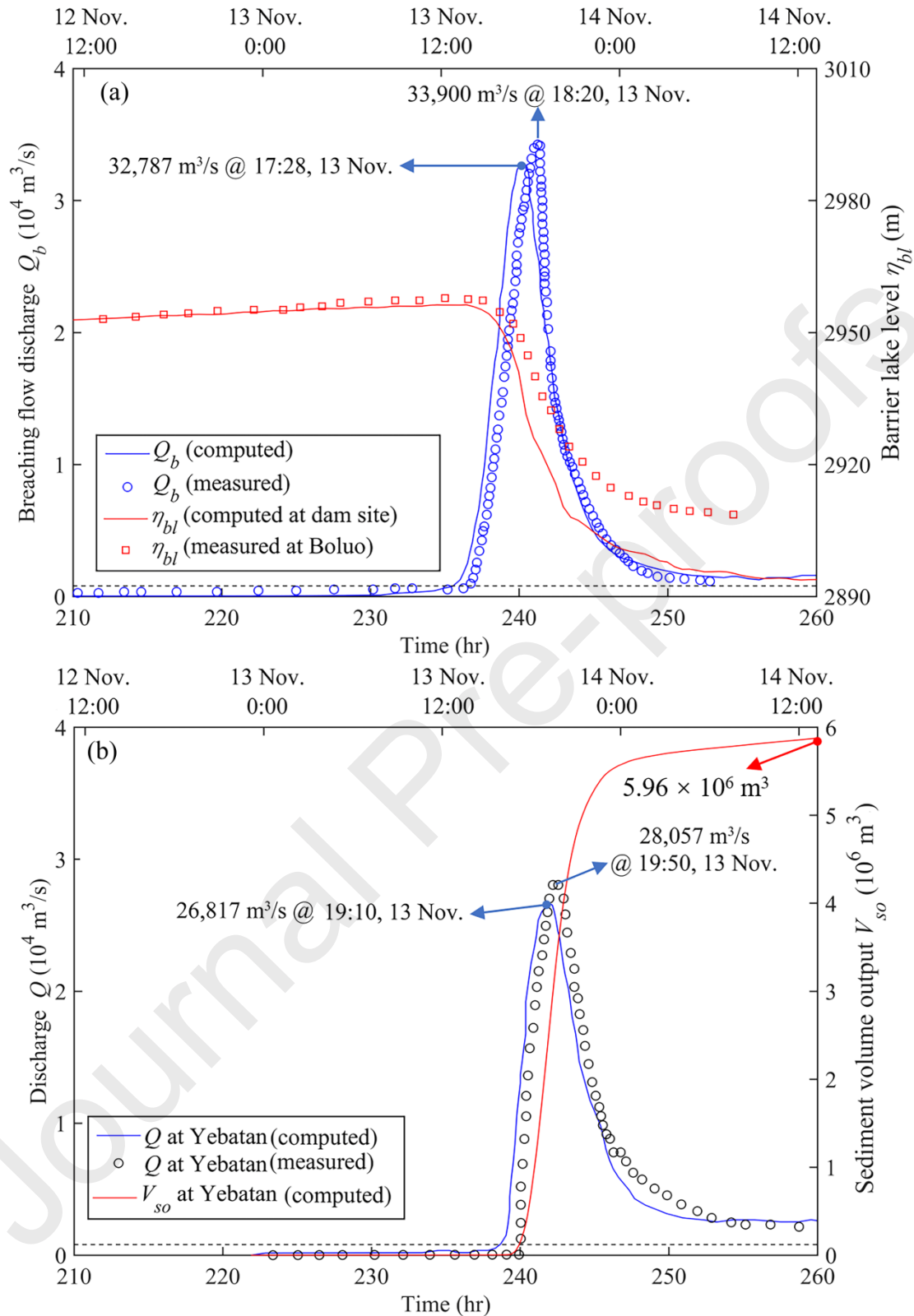
Fig. 19. (a) Breaching flow discharge hydrograph and water level time series at the "11.03" Baige landslide dam site; (b) flow discharge hydrograph and sediment volume output series at Yebatan (the downstream station): model predictions (solid lines) and measured data (open circles).

Fig. 20 presents contour plots of the evolution of the dam breach with instantaneous flow velocity vectors superimposed. At $t =$ 202.75 hr at 4:00 on 12 November (Fig. 20a), the water level of the barrier lake rises above the bed level of the artificial flood channel and overtopping commences. The overtopping flow then traverses the dam crest as an almost uniform sheet. The breach channel hardly widens, while the main dam body slightly erodes (Fig. 20b). During the next stage, breach channel enlarges slowly over a relatively long period (about 24 hrs). Meanwhile, the steepest section of the downstream face of the dam experiences significant erosion (Fig. 20c), which causes the flow velocity to increase locally. The resultant rapid flow in this steep section entrains further sediment and intensive scouring rapidly propagates backward toward the upstream area (Fig. 20d). Such headward erosion raises the breaching flow discharge (Fig. 19), leading to progressive vertical and horizontal enlargement of the breach channel (Fig. 20d and e). In general, breach deepening is associated with steepening of the sidewalls that may collapse once a critical failure angle is exceeded, leading to breach widening. In addition, the river channel downstream of the landslide dam accretes sediment scoured from the dam. The model indicates that high flow speeds, up to 15 m/s occur as the breaching flow discharge increases. Accordingly, both flow speed and bed erosion decrease as the barrier lake water level decreases and the river flow returns to base flow (Fig. 20f).
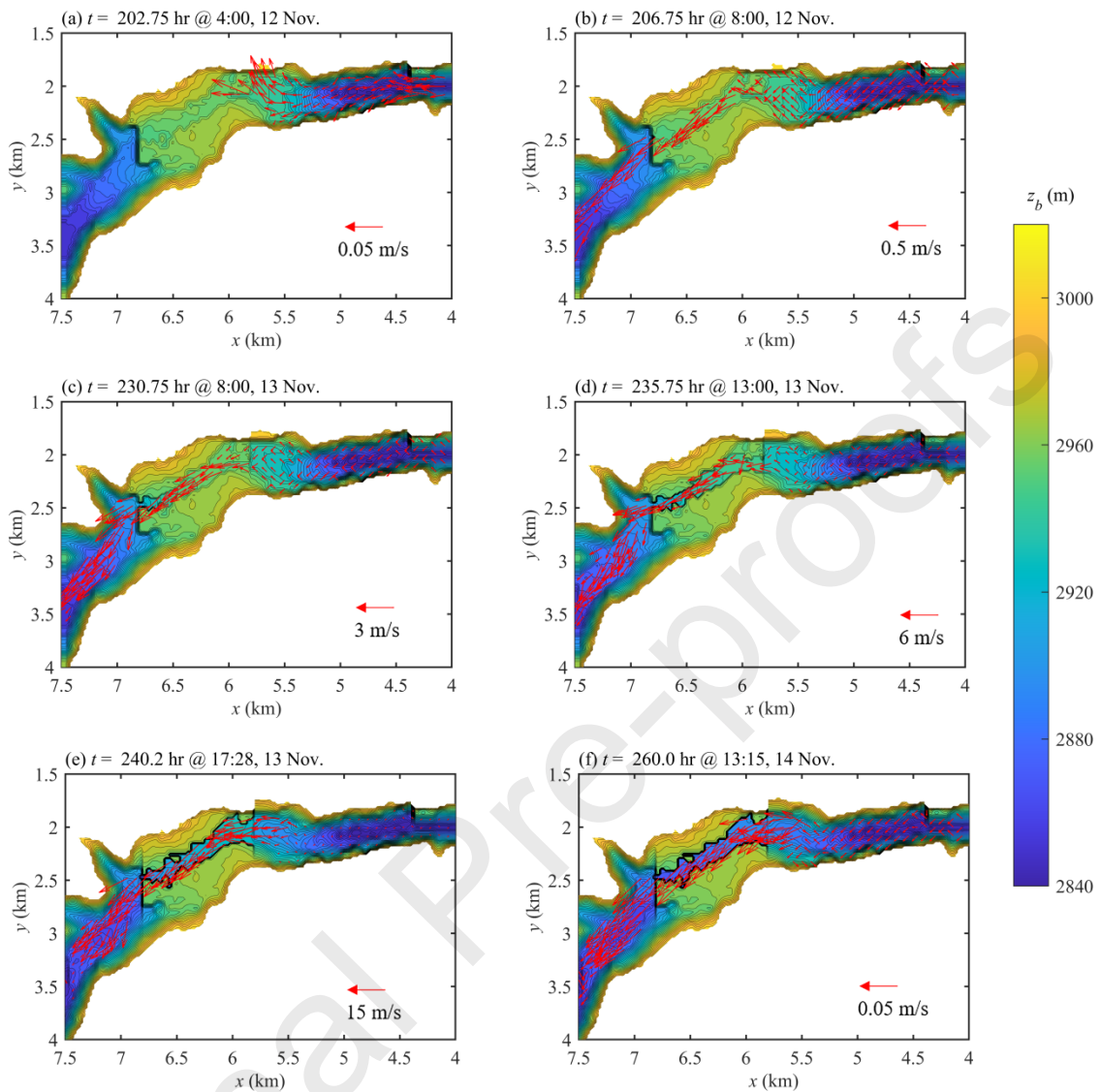
Fig. 20. "11.03" Baige landslide dam breach evolution depicted as bed deformation contours and superimposed flow velocity vectors at post-landslide times, t =: (a) 202.75 hr; (b) 206.75 hr; (c) 230.75 hr; (d) 235.75 hr; (e) 240.2 hr; and (f) 260.0 hr.

A further scenario is now considered for the case of the second landslide dam in the absence of an artificial flood channel. The computation automatically terminated once the river flow returned to base flow. Fig. 21 displays the predicted breach flow discharge hydrograph and barrier lake level time series. In the absence of an artificial flood channel, the

breaching process is significantly delayed, the peak discharge much larger, and the barrier lake level raised. This finding is qualitatively consistent with experimental observations from another landslide dam failure (Cao et al., 2011a). For a constant inflow discharge of 800 m³/s, the model estimates that 3 more days will be taken to fill the barrier lake and overtop the landslide dam (than for the case with the artificial channel present). In the absence of the channel, the model predicts that the peak breaching flow discharge would reach 51,884 m³/s (an increase of 58.2%) at 22:45 on 16 November, and the maximum water level of the barrier lake would attain 2967.5 m (an increase of 11.2 m). As would be expected, the model predicts that construction of an artificial flood channel would significantly alleviate downstream flood risk.
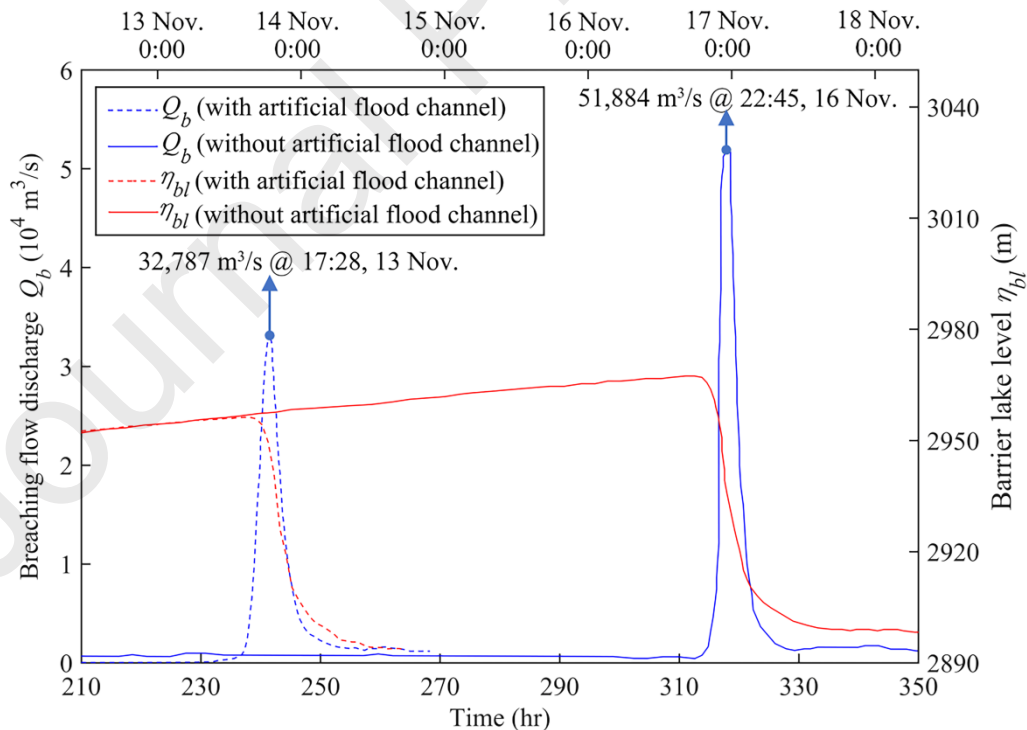

Fig. 21. Model predictions of breaching flow discharge hydrographs (blue) and barrier lake level time series (red): scenario with artificial flood channel (dashed lines); and scenario without an artificial flood channel (solid lines).

Table 5 summarizes the L^1 values of the model prediction for Baige barrier lake events, which quantitatively demonstrate that the computed results are in good agreement with the measured data. Furthermore, it shows that the error of the numerical solution accumulates and propagates within Phase I, from landslide dam and barrier lake formation, through to barrier lake outburst and downstream flooding, then extending to Phase II, in which a further propagation and accumulation can be observed.

Table 5 Summary of L^1 norms of model prediction for Baige barrier lake events

L^1	Phase I	Phase II
Landslide dam morphology L_{bd}^1	12.45%	22.38%
Breaching flow discharge hydrograph $L_{Q_b}^1$	15.31%	23.22%
Flow discharge hydrograph at Yebatan L_Q^1	15.85%	25.47%

5. Conclusions

The Baige barrier lake events of 2018 offers unique insight into landslide-induced multi-hazard chains that could produce catastrophic disasters extending far beyond the source zone. Based on a recent 2D double layer-averaged two-phase flow model, we reconstruct the whole process of the Baige barrier lake outburst flood within a single model run, encompassing landslide-generated waves, landslide dam and barrier lake formation, the barrier lake outburst, and the subsequent downstream flood. In terms of landslide-generated

waves, landslide dam morphology, stage time series and discharge hydrographs at the dam site and a downstream gauging station, the present model solutions are in good agreement with field observations. Construction of an artificial flood channel at the dam crest is demonstrated to be an effective mitigation strategy for downstream flood risk arising from a barrier lake outburst. The present work reveals the primary role of grains in landslide dam formation and also the dominant role of water in the barrier lake outburst and the resultant flood. Moreover, whilst small river flow discharge and large initial landslide volume favour landslide dam and barrier lake formation, they delay the occurrence time of the barrier lake outburst and its subsequent flood.

The present modelling framework offers considerable promise for assessing landslide-induced multi-hazard chains, and informing mitigation and adaptation strategies. Such an approach is particularly timely, given the increased instability of high mountain slopes and the accelerating trends in extreme precipitation amount, intensity and frequency of occurrence due to climate change, which are likely to trigger increasing numbers of landslides in the future. The modelling framework would achieve high computational efficiency by implementation of unstructured grids, parallel architecture and adaptive local-time-step techniques, thus supporting timely decision making in emergency response operation. Inevitably, the model incurs uncertainty arising from incomplete knowledge of the estimates of mass exchanges between the landslide and the bed, and interface and bed resistances. Therefore, systematic fundamental investigations are therefore recommended into the mechanisms associated with these exchanges and resistances.

Acknowledgements

References

Abadie, S., Harris, J.C., Grilli, S.T., Fabre, R., 2012. Numerical modeling of tsunami waves generated by the flank collapse of the Cumbre Vieja Volcano (La Palma, Canary Islands): Tsunami source and near field effects. J. Geophys. Res.-Oceans 117, C05030. http://dx.doi.org/10.1029/2011JC007646.

ASCE/EWRI Task Committee on Dam/Levee Breaching, 2011. Earthen embankment breaching. J. Hydraul. Eng. 137(12), 1549-1564. https://doi.org/10.1061/(ASCE)HY.1943-7900.0000498.

Bandara, S., Soga, K., 2015. Coupling of soil deformation and pore fluid flow using material point method. Comput. Geotech. 63, 199-214. https://doi.org/10.1016/j.compgeo.2014.09.009.

Cai, Y., Luan, Y., Yang, Q., Xu, F., Zhang, S., Shi, Y., Yidu, L., 2019. Study on structural morphology and dam-break characteristics of Baige barrier dam on Jinsha River. Yangtze River 50(3), 15-22 (in Chinese).

Cao, Z., Pender, G., Wallis, S., Carling, P., 2004. Computational dam-break hydraulics over erodible sediment bed. J. Hydraul. Eng. 130(7), 689-703. http://dx.doi.org/10.1061/(ASCE)0733-9429(2004)130:7(689).

Cao, Z., Yue, Z., Pender, G., 2011a. Landslide dam failure and flood hydraulics. Part I: experimental investigation. Nat. Hazards 59(2), 1003-1019. https://doi.org/10.1007/s11069-011-9814-8.

Cao, Z., Yue, Z., Pender, G., 2011b. Landslide dam failure and flood hydraulics. Part II: coupled mathematical modelling. Nat. Hazards 59(2), 1021-1045. https://doi.org/10.1007/s11069-011-9815-7.

Cao, Z., Yue, Z., Pender, G., 2011c. Flood hydraulics due to cascade landslide dam failure. J. Flood Risk Manag. 4(2), 104-114. https://doi.org/10.1111/j.1753-318X.2011.01098.x.

Cao, Z., Xia, C., Pender, G., Liu, Q., 2017. Shallow water hydro-sediment-morphodynamic equations for fluvial processes. J. Hydraul. Eng. 143(5), 02517001. http://dx.doi.org/10.1061/(ASCE)HY.1943-7900.0001281.

Carpignano, A., Golia, E., Di Mauro, C., Bouchon, S., Nordvik, J. P., 2009. A methodological approach for the definition of multi-risk maps at regional level: first application. J. Risk Res. 12(3-4), 513-534. https://doi.org/10.1080/13669870903050269.

Carrivick, J. L., 2010. Dam break-Outburst flood propagation and transient hydraulics: A geosciences perspective. J. Hydro. 380(3-4), 338-355. https://doi.org/10.1016/j.jhydrol.2009.11.009.

Chang, D. S., Zhang, L. M., 2010. Simulation of the erosion process of landslide dams due to overtopping considering variations in soil erodibility along depth. Nat. Hazard Earth Sys. 10(4), 933. https://doi.org/10.5194/nhess-10-933-2010.

Chen, C., Zhang, L., Xiao, T., He, J., 2020. Barrier lake bursting and flood routing in the Yarlung Tsangpo Grand Canyon in October 2018. J. Hydro. 583, 124603. https://doi.org/10.1016/j.jhydrol.2020.124603.

Corominas, J., van Westen, C., Frattini, P., Cascini, L., Malet, J.P., Fotopoulou, S., Catani, F., Van Den Eeckhaut, M., Mavrouli, O., Agliardi, F. and Pitilakis, K., 2014. Recommendations for the quantitative analysis of landslide risk. Bull. Eng. Geo. Environ. 73(2), 209-263. https://doi.org/10.1007/s10064-013-0538-8.

Costa, J. E., Schuster, R. L., 1988. The formation and failure of natural dams. Geol. Soc. Am. Bull. 100(7), 1054-1068. https://doi.org/10.1130/0016-7606(1988)100<1054:TFAFON>2.3.CO;2.

Cui, P., Zhou, G.G.D., Zhu, X.H., Zhang, J.Q., 2013. Scale amplification of natural debris flows caused by cascading landslide dam failures. Geomorphology 182, 173–189. https://doi.org/10.1016/j.geomorph.2012.11.009.

Dai, F. C., Lee, C. F., Deng, J. H., Tham, L. G., 2005. The 1786 earthquake-triggered landslide dam and subsequent dam-break flood on the Dadu River, southwestern China. Geomorphology 65(3-4), 205-221. https://doi.org/10.1016/j.geomorph.2004.08.011.

Davies, T. R., Manville, V., Kunz, M., Donadini, L., 2007. Modeling landslide dam break flood magnitudes: case study. J. Hydraul. Eng. 133(7), 713–720. https://doi.org/10.1061/(ASCE)0733-9429(2007)133:7(713).

Delaney, K. B., Evans, S. G., 2015. The 2000 Yigong landslide (Tibetan Plateau), rockslide-dammed lake and outburst flood: review, remote sensing analysis, and process modelling. Geomorphology 246, 377-393. https://doi.org/10.1016/j.geomorph.2015.06.020.

Donat, M. G., Alexander, L. V., Yang, H., Durre, I., Vose, R., Dunn, R. J. H., ... & Hewitson, B. (2013). Updated analyses of temperature and precipitation extreme indices since the beginning of the twentieth century: The HadEX2 dataset. J. Geophys. Res.-Atmospheres 118(5), 2098-2118. https://doi.org/10.1002/jgrd.50150.

Drake, T.G., Shreve, R.L., Dietrich, W.E., Whiting, P.J., Leopold, L.B., 1988. Bedload transport of fine gravel observed by motion-picture photography. J. Fluid Mech. 192, 193-217. https://dx.doi.org/10.1017/S0 0221120880 01831.

Ermini, L., Casagli, N., 2003. Prediction of the behaviour of landslide dams using a geomorphological dimensionless index. Earth Surf. Proc. Land. 28(1), 31-47. https://doi.org/10.1002/esp.424.

Faeh, R., 2007. Numerical modeling of breach erosion of river embankments. J. Hydraul. Eng. 133(9), 1000-1009. https://doi.org/10.1061/(ASCE)0733-9429(2007)133:9(1000).

Fan, X., Scaringi, G., Korup, O., West, A. J. et al., 2019a. Earthquake-induced chains of geologic hazards: Patterns, mechanisms, and impacts. Rev. Geophys. 57(2), 421-503. https://doi.org/10.1029/2018RG000626.

Fan, X., Xu, Q., Alonso-Rodriguez, A. et al., 2019b. Successive landsliding and damming of the Jinsha River in eastern Tibet, China: prime investigation, early warning, and emergency response. Landslides 16(5), 1003-1020. https://doi.org/10.1007/s10346-019-01159-x.

Fan, X., Yang, F., Subramanian, S. S. et al., 2020a. Prediction of a multi-hazard chain by an integrated numerical simulation approach: the Baige landslide, Jinsha River, China. Landslides 17(1), 147-164. https://doi.org/10.1007/s10346-019-01313-5.

Fan, X., Dufresne, A., Subramanian, S. S., Strom, A. et al. 2020b. The formation and impact of landslide dams–State of the art. Earth-Science Reviews, 103116. https://doi.org/10.1016/j.earscirev.2020.103116.

Fread, D. L., 1988. BREACH: an erosion model for earthen dam failure. U.S. Department of Commerce, National Oceanic and Atmospheric Administration, National Weather

Service, Office of Hydrology, Silver Spring, USA.

Ferguson, R. I., Wathen, S. J., 1998. Tracer-pebble movement along a concave river profile: virtual velocity in relation to grain size and shear stress. Water Resour. Res. 34 (8), 2031–2038. http://dx.doi.org/10.1029/98WR01283.

Hu, Y., Yu, Z., Zhou, J., 2020. Numerical simulation of landslide-generated waves during the 11 October 2018 Baige landslide at the Jinsha River. Landslides, 17, 2317–2328. https://doi.org/10.1007/s10346-020-01382-x.

Huang, W., Cao, Z., Yue, Z., Pender, G., Zhou, J. 2012. Coupled modelling of flood due to natural landslide dam breach. Proc. ICE Water Manag. 165, 525-542. https://doi.org/10.1680/wama.12.00017.

Lee, C. F., Dai, F. C., 2011. The 1786 Dadu River Landslide Dam, Sichuan, China, in: Evans, S., Hermanns, R., Strom, A., Scarascia-Mugnozza, G. (Eds.), Natural and Artificial Rockslide Dams. Springer, Berlin, Heidelberg, pp. 369-388. https://doi.org/10.1007/978-3-642-04764-0_13

Lenzi, M.A., 2004. Displacement and transport of marked pebbles, cobbles and boulders during floods in a steep mountain stream. Hydrol. Process 18 (10), 1899– 1914. http://dx.doi.org/10.1002/hyp.1456.

Leonardi, A., Wittel, F. K., Mendoza, M., Vetter, R., Herrmann, H. J., 2016. Particle-fluid-structure interaction for debris flow impact on flexible barriers. Comput-aided Civ. Inf. Eng. 31(5), 323-333. https://doi.org/10.1111/mice.12165.

Li, J., Cao, Z., Pender, G., Liu, Q., 2013. A double layer-averaged model for dam-break flows over mobile bed. J. Hydraul. Res. 51(5), 518-534. https://doi.org/10.1080/00221686.2013.812047.

Li, J., Cao, Z., Liu, Q., 2019. Waves and sediment transport due to granular landslides impacting reservoirs. Water Resour. Res. 55(1), 495-518. https://doi.org/:10.1029/2018WR023191.

Li, J., Cao, Z., Cui, Y., Borthwick, A., 2020. Barrier lake formation due to landslide impacting a river: A numerical study using a double layer-averaged two-phase flow model. Appl. Math. Model. 80, 574-601. https://doi.org/10.1016/j.apm.2019.11.031.

Liang, Q., Borthwick, A., 2009. Adaptive quadtree simulation of shallow flows with wet–dry fronts over complex topography. Comput. Fluids 38(2), 221-234.

http://dx.doi.org/10.1016/j.compfluid.2008. 02.008.

Liu, W., He, S., 2016. A two-layer model for simulating landslide dam over mobile river beds. Landslides 13(3), 565-576. https://doi.org/10.1007/s10346-015-0585-2.

Liu, W., He, S., 2018. Dynamic simulation of a mountain disaster chain: landslides, barrier lakes, and outburst floods. Nat. Hazards 90(2), 757-775. https://doi.org/10.1007/s11069-017-3073-2.

Miller, G. S., Andy Take, W., Mulligan, R. P., McDougall, S., 2017. Tsunamis generated by long and thin granular landslides in a large flume. J. Geophys. Res.- Oceans 122(1), 653-668. http://dx.doi.org/10.1002/2016JC012177.

Morris, J. F., 2009. A review of microstructure in concentrated suspensions and its implications for rheology and bulk flow. Rheol. Acta 48(8), 909-923. https://doi.org/10.1007/s00397-009-0352-1.

Morris, M. W., Kortenhaus, A., Visser, P. J., 2009. Modelling breach initiation and growth. FLOODsite Report T06-08-02, FLOODsite Project, HR Wallingford, UK.

O'Brien, J. S., Julien, P. Y., Fullerton, W. T., 1993. Two-dimensional water flood and mudflow simulation. J. Hydraul. Eng. 119(2), 244-261. https://doi.org/10.1061/(ASCE)0733-9429(1993)119:2(244).

Peng, M., Zhang, L. M., 2012. Breaching parameters of landslide dams. Landslides 9(1), 13-31. https://doi.org/10.1007/s10346-011-0271-y.

Pudasaini, S. P., 2012. A general two-phase debris flow model. J. Geophys. Res.- Earth Surf. 117(F3). https://doi.org/0.1029/2011JF002186.

Reeks, M. W., Hall, D., 2001. Kinetic models for particle resuspension in turbulent flows: theory and measurement. J. Aerosol Sci. 32(1), 1-31. https://doi.org/10.1016/S0021-8502(00)00063-X.

Shan, T., Zhao, J., 2014. A coupled CFD-DEM analysis of granular flow impacting on a water reservoir. Acta Mech. 225(8), 2449-2470. http://dx.doi.org/10.1007/s00707-014-1119-z.

Shang, Y., Yang, Z., Li, L., Liao, Q., Wang, Y., 2003. A super-large landslide in Tibet in 2000: background, occurrence, disaster, and origin. Geomorphology 54(3-4), 225-243. https://doi.org/10.1016/S0169-555X(02)00358-6.

Shi, C., An, Y., Wu, Q., Liu, Q., Cao, Z., 2016. Numerical simulation of landslide-generated waves using a soil–water coupling smoothed particle hydrodynamics model. Adv. Water Resour. 92, 130-141. https://doi.org/10.1016/j.advwatres.2016.04.002

Si, P., Aaron, J., McDougall, S., Lu, J., Yu, X., Roberts, N. J., Clague, J. J., 2018. A non-hydrostatic model for the numerical study of landslide-generated waves. Landslides 15(4), 711-726. https://doi.org/10.1007/s10346-017-0891-y.

Skvortsov, A., Bornhold, B., 2007. Numerical simulation of the landslide generated tsunami in Kitimat Arm, British Columbia, Canada, 27 April 1975. J. Geophys. Res.- Earth Surf. 112, F02028. https://doi.org/10.1029/2006JF000499.

Temple, D. M., Hanson, G. J., Neilsen, M. L., Cook, K. R., 2005. Simplified breach analysis model for homogeneous embankments: Part I, Background and model components, in: Proc. 25th Annual U.S. Society on Dams Conference, Denver, pp. 151-161.

United States Army Corps of Engineers (USACE), 2016. HEC-RAS, River Analysis System - Hydraulic Reference Manual (Version 5.0). https://www.hec.usace.army.mil/software/hec-ras/documentation.aspx (accessed 23 May 2020).

Van Asch, T. W., Buma, J., Van Beek, L. P. H., 1999. A view on some hydrological triggering systems in landslides. Geomorphology 30(1-2), 25-32. https://doi.org/10.1016/S0169-555X(99)00042-2.

Vetsch, D., Siviglia, A., Ehrbar, D., Facchini, M., Kammerer, S., Koch, A., Peter, S., Vonwiller, L., Gerber, M., Volz, C., Farshi, D., Mueller, R., Rousselot, P., Veprek, R., Faeh, R., 2018. System Manuals of BASEMENT, Version 2.8. http://www.basement.ethz.ch (accessed 23 May 2020).

Walder, J. S., O'Connor, J. E., 1997. Methods for predicting peak discharge of floods caused by failure of natural and constructed earthen dams. Water Resour. Res. 33(10), 2337-2348. https://doi.org/10.1029/97WR01616.

Wang, W., Chen, G., Zhang, Y., Zheng, L., Zhang, H., 2017. Dynamic simulation of landslide dam behavior considering kinematic characteristics using a coupled DDA-SPH method. Eng. Anal. Bound. Elem. 80, 172-183. https://doi.org/10.1016/j.enganabound.2017.02.016.

Wang, W., Yin, K., Chen, G., Chai, B., Han, Z., Zhou, J., 2019. Practical application of the

coupled DDA-SPH method in dynamic modeling for the formation of landslide dam. Landslides 16(5), 1021-1032. https://doi.org/10.1007/s10346-019-01143-5.

Wang, G., Liu, F., Fu, X., Li, T., 2008. Simulation of dam breach development for emergency treatment of the Tangjiashan Quake Lake in China. Sci. China Technol. Sci. 51(2), 82-94. https://doi.org/10.1007/s11431-008-6019-9.

Wang, Z., Bowles, D. S., 2006a. Three-dimensional non-cohesive earthen dam breach model. Part 1: Theory and methodology. Adv. Water Resour. 29(10), 1528-1545. https://doi.org/10.1016/j.advwatres.2005.11.009.

Wang, Z., Bowles, D. S., 2006b. Three-dimensional non-cohesive earthen dam breach model. Part 2: Validation and applications. Adv. Water Resour. 29(10), 1490-1503. https://doi.org/10.1016/j.advwatres.2005.11.010.

Wilcock, P. R., 1997. Entrainment, displacement and transport of tracer gravels. Earth Surf. Proc. Land. 22 (12), 1125–1138. http://dx.doi.org/10.1002/(SICI) 1096-9837(199712)22:12 <1125 .

Worni, R., Huggel, C., Clague, J. J., Schaub, Y., Stoffel, M., 2014. Coupling glacial lake impact, dam breach, and flood processes: A modeling perspective. Geomorphology 224, 161-176. https://doi.org/10.1016/j.geomorph.2014.06.031.

Wu, W., 2013. Simplified physically based model of earthen embankment breaching. J. Hydraul. Eng. 139(8), 837-851. https://doi.org/10.1061/(ASCE)HY.1943-7900.0000741.

Wu, W., Marsooli, R., He, Z., 2012. Depth-averaged two-dimensional model of unsteady flow and sediment transport due to noncohesive embankment break/breaching. J. Hydraul. Eng. 138(6), 503-516. https://doi.org/10.1029/2017WR022492.

Wu, Y., Fang, H., Huang, L., Ouyang, W., 2020. Changing runoff due to temperature and precipitation variations in the dammed Jinsha River. J. Hydrol. 582, 124500. https://doi.org/10.1016/j.jhydrol.2019.124500.

Xu, Q., Fan, X. M., Huang, R. Q., Van Westen, C., 2009. Landslide dams triggered by the Wenchuan Earthquake, Sichuan Province, south west China. Bull. Eng. Geol. Environ. 68(3), 373-386. https://doi.org/10.1007/s10064-009-0214-1.

Xu, W. J., Yao, Z. G., Luo, Y. T., Dong, X. Y., 2020. Study on landslide-induced wave disasters using a 3D coupled SPH-DEM method. Bull. Eng. Geol. Environ. 79(1), 467-483. https://doi.org/10.1007/s10064-019-01558-3.

Xu, Y., Zhang, L. M., 2009. Breaching parameters for earth and rockfill dams. J. Geotech. Geoenviron. Eng. 135(12), 1957-1970. https://doi.org/10.1061/(ASCE)GT.1943-5606.0000162.

Zhao, T., Dai, F., Xu, N. W., 2017. Coupled DEM-CFD investigation on the formation of landslide dams in narrow rivers. Landslides 14(1), 189-201. https://doi.org/10.1007/s10346-015-0675-1.

Zhang, L., Xiao, T., He, J., Chen, C., 2019. Erosion-based analysis of breaching of Baige landslide dams on the Jinsha River, China, in 2018. Landslides 16(10), 1965-1979. https://doi.org/10.1007/s10346-019-01247-y.

Zhang, Y., Meng, X. M., Dijkstra, T. A., Jordan, C. J., Chen, G., Zeng, R. Q., Novellino, A., 2020. Forecasting the magnitude of potential landslides based on InSAR techniques. Remote Sens. Environ. 241, 111738. https://doi.org/10.1016/j.rse.2020.111738.

Zhang, Z., He, S., Liu, W., Liang, H., Yan, S., Deng, Y., Bai, X. Chen, Z., 2019. Source characteristics and dynamics of the October 2018 Baige landslide revealed by broadband seismograms. Landslides 16(4), 777-785. https://doi.org/10.1007/s10346-019-01145-3

Zhong, Q., Chen, S., Wang, L., Shan, Y., 2020. Back analysis of breaching process of Baige landslide dam. Landslides, in press. https://doi.org/10.1007/s10346-020-01398-3

Zitti, G., Ancey, C., Postacchini, M., Brocchini, M., 2016. Impulse waves generated by snow avalanches: momentum and energy transfer to a water body. J. Geophys. Res.- Earth Surf. 121(12), 2399-2423. https://doi.org/10.1002/2016JF003891.

List of figure captions

Fig. 1. Location of Baige barrier lake, Jinsha River, China (adapted from Fan et al., 2020a): (a) upstream areas inundated by barrier lake; (b) towns affected by downstream flooding (the orange box indicates the study area).

Fig.2. "10.10" Baige barrier lake: (a) formation; (b) after breaching. (photo courtesy of Chinanews.com).

Fig. 3. "11.03" Baige barrier lake: (a) formation; (b) with artificial flood channel; (c) during breaching; (d) after breaching (photo courtesy of a CCTV.com; b Red Star News; c Ministry of Emergency Management of China; d L. Zhang et al., 2019).

Fig. 4. Phase I "10.10" Baige landslide impacting Jinsha river: model predictions of landslide velocity field at times $t =$ (a) 5 s, (b) 10 s, (c) 20 s, (d) 40 s, (e) 100 s, and (f) 900 s.

Fig. 5. Phase I "10.10" Baige landslide-generated waves: predicted water level hydrographs at three locations in the Jinsha river near Baige, Sichuan, China.

Fig. 6. "10.10" Baige landslide dam geometry: (a) bed deformation at $t =$ 900 s predicted by present model; and (b) cross-section profile of landslide dam in the original river stream-wise direction (A-A'): model prediction (solid line) and measured data from Fan et al. (2020a) (dashed line).

Fig. 7. "10.10" Baige landslide dam and barrier lake formation: (a1-a6) depth of water layer; (b1-b6) landslide thickness; and (c1-c6) bed deformation.

Fig. 8. (a) Breaching flow discharge hydrograph and (b) flow discharge hydrograph and sediment volume output time series at the Yabatan gauging station: model predictions (solid lines) and measured data from Cai et al. (2019) (open black circles).

Fig. 9. Water level time series at the barrier lake and selected sites downstream of the "10.10" Baige landslide dam.

Fig. 10. "10.10" Landslide-induced barrier lake outburst and the resultant flood: (a1-a6) depth of water layer; (b1-b6) water-sediment mixture thickness; and (c1-c6) bed deformation. (a1, b1 and c1) Landslide dam is overtopped naturally and dam breach commences. (a2, b2 and c2) Breaching flow arrives at Yebatan. (a3, b3 and c3) Breaching flow discharge is almost equivalent to upstream inflow discharge. (a4, b4 and c4) Breaching flow peaks. (a5, b5 and c5) Peak breaching flow arrives at Yebatan. (a6, b6 and c6) Jinsha river resumes its base flow and the dam breach process terminates.

Fig. 11. Contour plots of velocity difference between water and sediment phases of the water-sediment mixture flow layer in the transverse ($y-$axis) direction at different times from 10 s to 55.75 hr after the start of the "10.10" Baige landslide: a1–a5 with $d=$ 1 mm; and b1–b5 with $d=20$ mm.

Fig. 12. Contour plots of velocity difference between water and sediment phases of the water-sediment mixture flow layer in the longitudinal ($x-$axis) direction at different times from 10 s to 55.75 hr after the start of the "10.10" Baige landslide, a1-a5 with $d=$ 1 mm, and b1-b5 with $d=20$ mm.

Fig. 13. Model predictions of breaching flow discharge hydrographs for three different Jinsha river inflow discharges.

Fig. 14. Model predictions of breaching flow discharge hydrographs for three different initial landslide volumes.

Fig. 15. "10.10" Baige landslide dam morphology assuming different bed friction coefficient $\tan\delta$ (a1-a3) bed deformation at $t=$ 900 s predicted by present model; and (b1-b3) cross-section profile of landslide dam in the original river stream-wise direction (A-A'): model prediction (solid line) and measured data from Fan et al. (2020a) (dashed line).

Fig. 16. "10.10" Baige landslide dam morphology assuming different Manning roughness coefficient n_b (a1-a3) bed deformation at $t =$ 900 s predicted by present model; and (b1-b3) cross-section profile of landslide dam in the original river stream-wise direction (A-A'): model prediction (solid line) and measured data from Fan et al. (2020a) (dashed line).

Fig. 17. Model predictions (solid lines) of breaching flow discharge hydrographs assuming (a) different bed friction coefficient $\tan\delta$; and (b) different Manning roughness coefficient n_b and measured data (open circles) from Cai et al. (2019).

Fig. 18. "11.03" Baige landslide dam geometry: (a) predicted bed deformation contours at $t =$ 900 s; and (b) predicted (solid line) and measured (dashed line, Fan et al. 2020a) cross-sectional profiles of the landslide dam in a longitudinal direction along the river (B-B').

Fig. 19. (a) Breaching flow discharge hydrograph and water level time series at the "11.03" Baige landslide dam site; (b) flow discharge hydrograph and sediment volume output series at Yebatan (the downstream station): model predictions (solid lines) and measured data (open circles).

Fig. 20. "11.03" Baige landslide dam breach evolution depicted as bed deformation contours and superimposed flow velocity vectors at post-landslide times, $t =$: (a) 202.75 hr; (b) 206.75 hr; (c) 230.75 hr; (d) 235.75 hr; (e) 240.2 hr; and (f) 260.0 hr.

Fig. 21. Model predictions of breaching flow discharge hydrographs (blue) and barrier lake level time series (red): scenario with artificial flood channel (dashed lines); and scenario without an artificial flood channel (solid lines).

List of table captions

Table 1 "10.10" Baige landslide-generated wave run-up on the opposite bank

Table 2 Summary of "10.10" Baige landslide dam morphology

Table 3 Predicted effect of inflow discharge on landslide dam formation, overtopping, and breaching processes (Series 1 tests)

Table 4 Predicted effect of inflow landslide volume on landslide dam formation, overtopping, and breaching processes (Series 2 tests)

Table 5 Summary of L^1 norms of model prediction for Baige barrier lake events

CRediT author statement

Ji Li: Software, Data curation, Investigation, Writing- Original draft preparation.

Zhixian Cao: Conceptualization, Methodology, Investigation, Writing- Reviewing and Editing, Supervision.

Yifei Cui: Conceptualization, Investigation, Writing- Original draft preparation.

Xuanmei Fan: Data curation, Investigation, Writing- Original draft preparation.

Wenjun Yang: Data curation, Investigation.

Wei Huang: Data curation, Investigation.

Alistair Borthwick: Methodology, Investigation, Writing- Reviewing and Editing.

Highlights:

- The 2018 Baige landslide-induced barrier lake on the Jinsha River is investigated

- The whole process is well reconstructed by a single 2D model for the first time

- An artificial flood channel effectively alleviated downstream flood risk

- Grains drive water during landslide dam formation, but water governs the outburst

- Effects of upstream inflow discharge and initial landslide volume are revealed